UNIVERSITÀ DEGLI STUDI DI PADOVA

UNIVERSITÀ DEGLI STUDI DI PADOVA
Dipartimento di Ingegneria Industriale DII
Corso di Laurea Magistrale in Ingegneria Aerospaziale

COMPUTATIONAL FLUID DYNAMICS STUDY OF AN ADVANCED HIGH-SPEED NASA PROPELLER

Relatore: Prof. Andrea Magrini

Laureando: Andrea Pacilli, 2037809

Anno Accademico 2023/2024

ABSTRACT

Turbo-prop engines have high propulsive efficiency for moderate subsonic cruise speed. However, their performance rapidly deteriorates as transonic conditions are approached. NASA, through the "Advanced Turboprop Project" (ATP), developed advanced propellers capable of operating at high cruise Mach number, known as prop-fan. This thesis focuses on a Computational Fluid Dynamics (CFD) study of SR-3 NASA high speed propeller to investigate the reliability of the numerical model in reproducing experimental performance data at a cruise Mach number of 0.80. The reconstructed blade geometry is simulated using Ansys CFX on a range of advance ratios from 2.9 to 4.1. The results obtained are compared with experimental data provided by NASA; the maximum efficiency obtained from the simulation is 70.9%, compared to the experimentally one 78.2%. In general, efficiency is lower compared to the NASA test cases due to the overestimation of the power coefficient. At an advance ratio of 3.06, the power coefficient is 2.40, whereas the wind tunnel datum is 1.86. As the advance ratio increases, this discrepancy decreases, and the data tends to be more similar to the experimental ones.

SOMMARIO

I motori turboelica hanno un'alta efficienza propulsiva per velocità di crociera subsoniche moderate. Tuttavia, le loro prestazioni si deteriorano rapidamente man mano che si avvicinano alle condizioni transoniche. La NASA, attraverso l'"Advance Turboprop Project" (ATP), ha sviluppato eliche avanzate capaci di operare ad elevati numeri di Mach in crociera, note come prop-fan. Questa tesi si concentra su uno studio di Dinamica dei Fluidi Computazionale (CFD) dell'elica ad alta velocità SR-3 della NASA per studiare l'affidabilità del modello numerico nel riprodurre i dati sperimentali delle prestazioni a un numero di Mach in crociera di 0.80. La geometria della paletta ricostruita è simulata utilizzando Ansys CFX su un range di rapporti di avanzamento da 2.9 a 4.1. I risultati ottenuti sono confrontati con i dati sperimentali forniti dalla NASA; l'efficienza massima ottenuta dalle simulazioni è del 70.9%, contro quella sperimentale del 78.2%. In generale, l'efficienza è minore rispetto ai casi dei test NASA a causa della sovrastima del power coefficient. Ad advance ratio 3.06 il power coefficient è 2.40, mentre il dato della galleria del vento è 1.86. All'aumentare dell'advance ratio tale discrepanza si riduce e i dati tendono ad essere più simili a quelli sperimentali.

CONTENTS

LIST OF FIGURES

LIST OF TABLES

ABBREVIATIONS

ATP Advanced Turboprop Project.

CFD Computational Fluid Dynamics.

MRF Moving reference frame.

RANS Reynolds Averaged Navier Stokes.

SR Single rotation.

SST Shear Stress Transport.

NOMENCLATURE

A Area.

B Number of blades.

C_d Drag coefficient for a blade section.

C_l Lift coefficient for a blade section.

C_p Power coefficient.

C_q Torque coefficient.

C_t Thrust coefficient.

D Propeller diameter.

E Efficiency.

J Advance ratio.

M Mach number.

P Power required.

P/A Power loading.

P_a Atmospheric pressure.

P_d Dynamic pressure.

P_s Static pressure.

P_t Total Pressure.

Q Torque.

T Propeller thrust.

T/A Disc loading.

T_0 Temperature.

V Flight speed.

V_R Relative flow speed.

Δ Sweep angle.

$\dot{m}$ Mass flow.

α angle of attack.

β Twist angle.

η_f Froude efficiency.

η_p Efficiency.

ω angular velocity.

ρ air density.

σ_R Palar solidity.

a Sound speed.

c Chord.

d Drag per unit length.

l Lift per unit length.

n number of revolutions.

r Radius.

s Span.

a Axial inflow factor.

b Slipstream factor.

v Induced disc speed.

1 Introduction

The need to find a solution to counteract the increase in oil prices in 1973 led the US government and NASA to establish the Advanced Turboprop Project (ATP) [10]. In this program, the goal was to develop innovative propeller configurations mounted in propulsion systems known as prop-fan. These engines are capable of operating in the high subsonic regime while maintaining high efficiency, low operating costs, and lower fuel consumption. The first propeller that NASA developed in the program was the SR-1. The objective was to demonstrate that prop-fan technology was as efficient as believed. The designers of the SR-1 tried to use every technique possible to reduce compressibility losses. Better airfoils were selected and blades with smaller thickness-to-chord ratios than conventional propellers were designed. The number of blades was increased to keep the diameter of the propeller smaller. Additionally, a sweep angle of 30° at the tip was used to reduce compressibility losses. With these characteristics, efficiencies of 77% at Mach 0.8 were achieved by the SR-1. Other propellers such as the SR-1M, SR-2, and SR-3 were developed from this model. Modifications to the twist angle and sweep angle were made in all these models. The sweep applied to the SR-3 was 45° for both aerodynamic and acoustic purposes. The results of the SR-3 tests, which achieved efficiencies of 79%, supported the performance expectations of NASA. This formed the basis for continuing research on prop-fan technology. In this chapter, the propeller will be briefly introduced, with reference to the main parameters that characterize it, including a section regarding the high-speed propeller and the prop-fan. Subsequently, the methods useful for this study will be outlined, and the main results obtained will be reported. Finally, conclusions will be presented, stating possible future developments. The main objective of this thesis concerns the development and validation of a CFD model that replicates experimental studies conducted by NASA on an advanced propeller known as the prop-fan and referred to by the agency as SR-3.

1.1 Fundamentals of propellers

In aeronautics, an aircraft propeller is a device that converts the rotational motion of the engine (such as a piston engine, electric engine or turboprop) into a propulsive force by accelerating the flow of air around it. As the propeller rotates, it generates thrust by accelerating a large volume of air through a small change in velocity, and this is a crucial point to be discussed later. In the case of a piston or electric engine, all of the thrust is generated by the propeller, whereas in the case of a turboprop the propeller generates 70% - 80% of the thrust and the remaining thrust is generated by the jet [1]. The propeller is very similar to a wing (in fact, a propeller has the shape of a typical airfoil section, as shown in the figure 1.1), but there is an important main difference: a wing translates, instead a propeller is characterised by a speed that depends on the radius. The dependence of the speed on the radius has important implications for the aerodynamic performance and structural design of the propeller, which will be discussed in the following chapters.

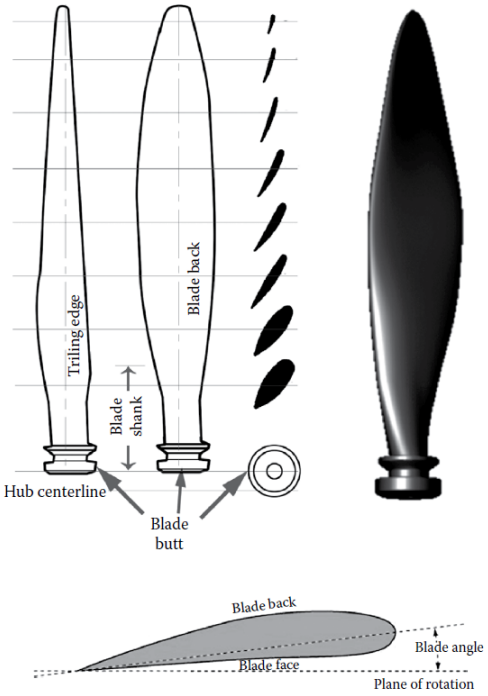

Figure 1.1: Propeller cross section
[1]

1.1.1 Types of propeller

Propellers can have fixed pitch or variable pitch. Pitch is an important parameter that defines how far a propeller can travel in one complete revolution. So, let's take a closer look about the pitch:

- Fixed pitch: the blades are fixed to the hub at a fixed angle that cannot be changed during flight (sometimes it can only be changed on the ground).
- Variable pitch: the pitch changes both on the ground and in flight and this type of propeller is used in larger and more sophisticated aircraft. In this case, variable pitch propellers are divided into two further categories, namely the *two-position propeller* and the *adjustable pitch propeller*. The first one allows the pitch to change into two angles, for example for low speed operations such as take-off and climb, or high speed operations such as cruising; the second one allows the pitch to change in flight by the pilot or with an automatic mechanism that adjusts the pitch according to the aircraft's speed.

The variable pitch propeller requires a mechanism that can be more complicated and heavier than a fixed pitch propeller. The main advantage of the variable pitch is that it allows the propeller to adapt to different flight conditions, reducing the loss of efficiency [1]. In an aircraft, the function of the variable pitch is therefore to keep the number of revolutions constant in order to maintain optimum performance over a wide range of operating conditions. In a commercial aviation aircraft, the mechanism used to change the pitch is a hydraulic system, whereas in an ultralight aircraft a stepper motor is used. In the

figure below, you can see the effect of pitch: at a high pitch, the propeller will travel further for the same number of revolutions than at a low pitch.

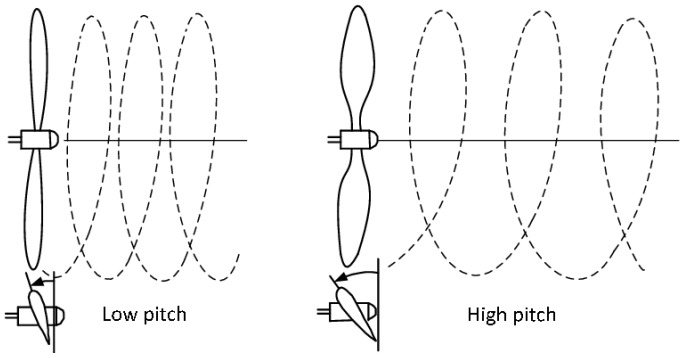

Figure 1.2: Influence of propeller pitch
[26]

For the sake of accuracy, it should be specified that the pitch discussed so far is the geometric pitch. In reality, the distance travelled after a complete revolution is called the real pitch or advancement or effective pitch. The difference between the geometric pitch and the real pitch is called the regress or slip (see figure 1.3 for clarity).

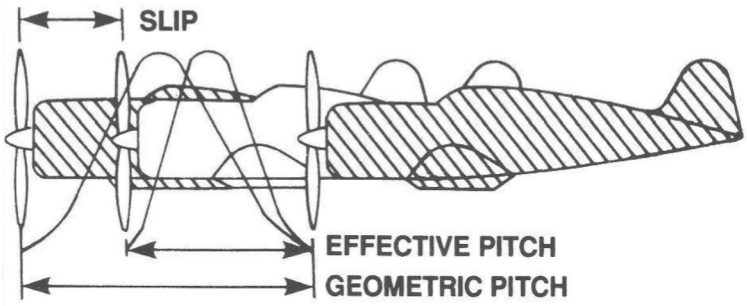

Figure 1.3: Real pitch vs geometric pitch
[27]

Generally, an efficient propeller has a small regress and therefore the geometric and actual pitch are very similar to each other. It is important not to associate geometric and real pitch with propeller efficiency, as the latter depends on the ratio between the power produced by the propeller and the power generated by the motor to turn the propeller.

1.1.2 Propeller parameters

Propeller efficiency is the most important parameter to consider when designing a propeller. But before talking about efficiency, other fundamental parameters should be introduced. There are several dimensionless variables to take into account when defining the performance of a propeller that is:

- **Power coefficient**:
$$C_p = \frac{P}{\rho n^3 D^5}$$
- **Thrust coefficient**:
$$C_t = \frac{T}{\rho n^2 D^4}$$
- **Torque coefficient** :
$$C_q = \frac{Q}{\rho n^2 D^5}$$
- **Advance ratio**:
$$J = \frac{V}{nD}$$
- **Efficiency**:
$$E = J\frac{Ct}{Cp}$$

From these parameters, it is possible to draw some important graphs that define more clearly how a propeller works.

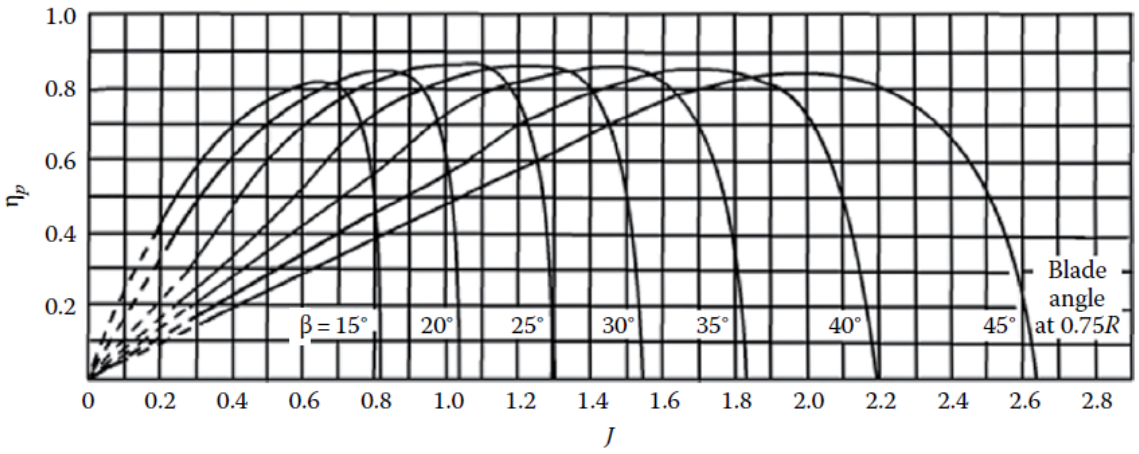

Figure 1.4: Efficiency vs advance ratio for a two-bladed propeller
[2]

In the figure (1.4) it can be seen the importance of the propeller pitch; as mentioned above, it allows to maintain maximum efficiency in different flight conditions (i.e. at different advance ratio). For example, let's take a look at the curve with 35° pitch and, imagine increasing the speed. If had not the possibility to change the pitch, efficiency would collapse, but thanks to the variable pitch it's possible to go from 35° to 40° and achieve the maximum efficiency at that speed, and so on in every conditions.

In the following figures, the other two fundamental parameters can be seen. The thrust coefficient (graph 1.5) describes the thrust the propeller is developing and it is higher at high pitch and low advance ratio. Finally, the power coefficient describes the amount of power that is required to make the propeller turn. It is interesting to note that the thrust coefficient goes to zero before the power coefficient, because power is still being consumed to spin the propeller. In the graph 1.6, the Ct curves are iso-thrust coefficient curves.

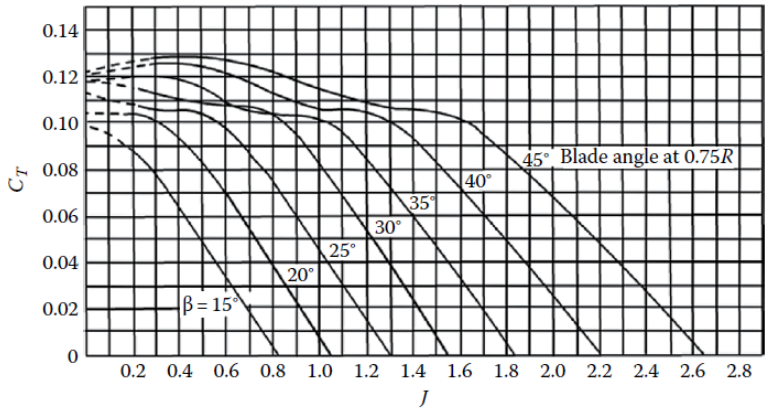

Figure 1.5: Thrust coefficients vs advance ratio for a two-bladed propeller [2]

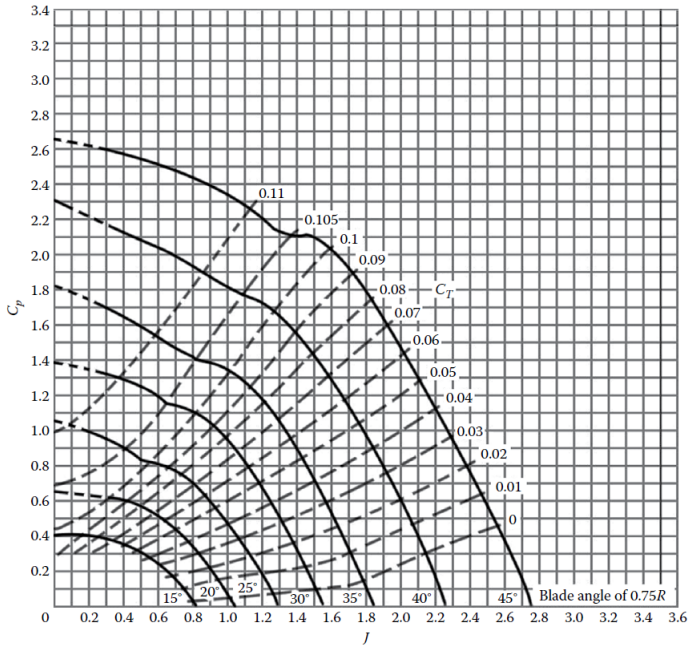

Figure 1.6: Power coefficient vs advance ratio for a two-bladed propeller [2]

1.2 High speed propeller

The conventional propellers installed in turboprop engines allow for efficiency levels close to 80% up to Mach 0.5, but they can experience efficiency drops beyond this Mach number due to compressibility losses. These losses are attributed to the use of relatively thick propellers in most propulsion systems operating with high helical tip Mach numbers. High-speed propellers installed in prop-fan engines manage to delay the effects of compressibility and maintain high performance at least up to Mach 0.8. Such propellers exhibit a set of unique characteristics that differentiate them from conventional ones. The main properties of high-speed propellers include blade sweep to reduce local Mach numbers and the use of thin profiles (especially at the tip) to mitigate drag rise Mach numbers. Additionally, to maintain a reasonable diameter, typically 8-12 blades are used [14].

1.2.1 Propfan

The prop-fan are propulsion systems tested by NASA in the early 1980s [10], designed to have a higher bypass ratio than turbofan while maintaining their efficiency even at high speeds. They have various configurations and represent a hybrid between a turboprop and a turbofan. Below, a table (1.7) is provided listing the main differences between a turboprop and a propfan.
However, one of the main problems of the propfan is the noise it generates. There are many studies aimed at finding solutions to reduce it. Indeed, a significant portion of the work carried out by NASA in the ATP program on this propulsion technology concerns the study of noise. [6]. Some methods to reduce it may be to increase the distance between the two propellers to reduce the effects of vortex interference at the tip of the blades, or to use a different number of blades between the front and the rear propeller, in order to avoid the resonance problem caused by identical propellers (i.e., with the same number of blades) [11].

Engine	Turboprop	Propfan
Number of blades	3–6	8–12
Diameter	Large	Smaller
Power/Square of diameter	Small	Larger
Blade shape	Nearly straight	Swept or scimitar-like profile
Maximum thickness	Thick	Thinner
Tip speed	Subsonic	Supersonic
BPR	Nearly 50	25 or more
Propulsive efficiency	High	Higher
ESFC(kg/hp·h)	0.19–0.23	0.17
Mach number	0.5–0.6	0.68
Cruise altitude	6000 m	11,000 m

Figure 1.7: Differences between turboprop and propfan
[1]

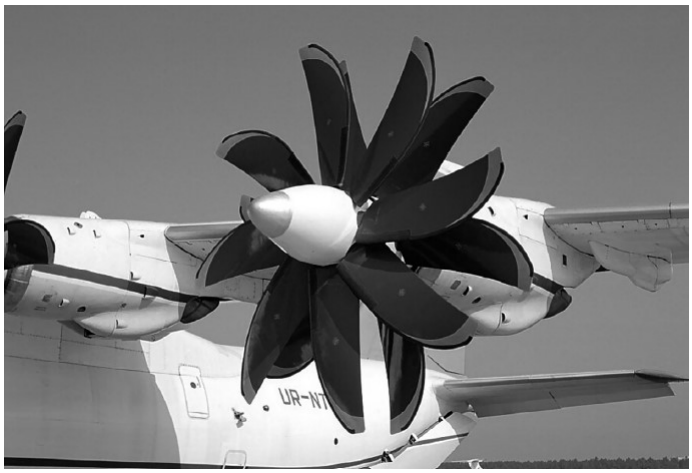

Figure 1.8: Antonov AN-70 Propfan
[1]

1.2.2 Fuel consumption and efficiency

The graph in the figure 1.9 shows the typical trend in the specific consumption of different engine types, in which it can be seen that turboprop and propfan engines are by far the most efficient at low flight speeds.

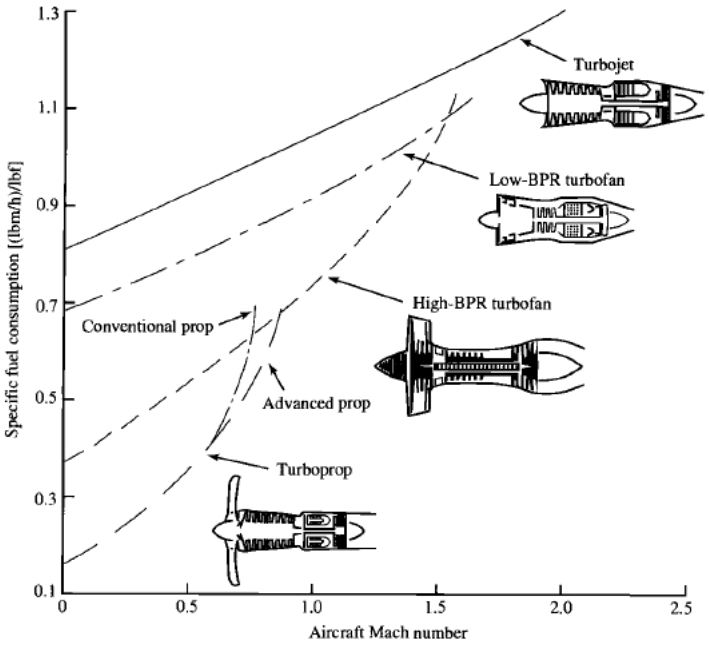

Figure 1.9: Fuel consumption of different engine types
[5]

Figure 1.10 shows the propulsive efficiency of turboprop, propfan, turbofan and turbojet on varying flight Mach in which, up to Mach 0.5, propeller-driven engines manage to be much more efficient even than turbofan. From the same figure, it is observed the efficiency trend of propfan, where the difference with respect to a turboprop is simply the type of propeller, as already explained in the previous paragraphs.

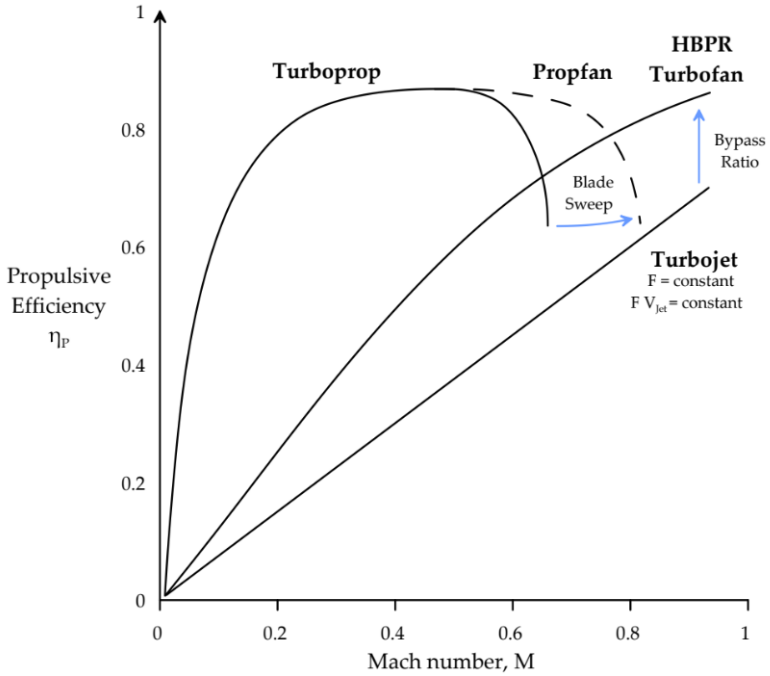

Figure 1.10: Efficiency of different engine types
[23]

2 MATERIALS AND METHODS

In this chapter the case study under consideration concerns a propeller developed and studied by NASA in the 1980s, in particular the propeller named by the space agency as SR-3 will be discussed, describing the methods used to derive its performance parameters.

2.1 NASA SR-3 propeller

This propeller is characterized by a unique design intended to maintain efficiency and reduce the generated noise even at high flight speeds. Actually, there are several types of propellers that tested by NASA (e.g. SR-1, SR-2, SR-5) but they all have the same purpose. Figures 2.1 and 2.2 show the SR-3 and SR-5 propellers respectively as examples.
The SR-3 propeller was designed by NASA with the aim of operating in cruise condition at Mach 0.8 with J=3.06, Cp=1.86 and efficiency close to 81% at an altitude of 10668 [m], diameter 0.622 [m] and a tip speed of 244 [m/s]. The propeller is characterised by 8 blades with a sweep angle of 45° at the tip; the sweep angle is useful to reduce all the negative effects of high speed, and in addition, the pitch is variable and the profiles that make up the blade are very thin, especially at the tip. Hence, the combination of small diameter, thin profiles with high sweep angle and variable pitch are all expedients that reduce losses due to compressibility phenomena.
Before talking about the SR-3 specifically, it is important to introduce some theoretical concepts about the propeller.

Figure 2.1: SR-3 propeller
[24]

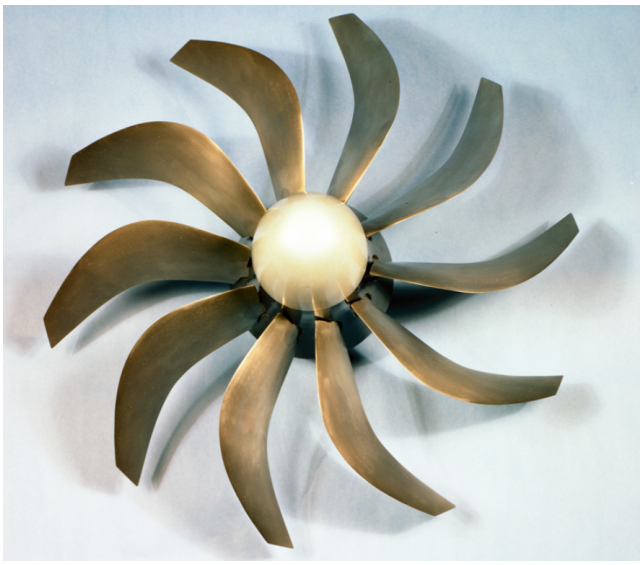

Figure 2.2: SR-5 propeller
[25]

2.2 Propeller theory

2.2.1 Actuator disk theory

The actuator disk theory defines the performance of a propeller. This theory does not consider the propeller as a series of blades but as a disk which processes airflow and generates a pressure gradient. However, it is important to note that this disk is a mathematical model that does not exist in reality. The actuator disk theory is based on some fundamental assumptions:

1. The fluid is isoentropic (no viscous losses, shock waves, etc...)
2. The fluid is incompressible (low Mach numbers)
3. The motion is quasi one-dimensional (i.e., quantities are uniform in the section, only axial velocity and acceleration are considered); therefore, if the flow accelerates, the area must decrease because $\dot{m} = \rho V A$
4. The rotation imparted to the flow is neglected
5. Pressure upstream, downstream, and outside the flow tube is constant

Referring to figure 2.3, which represents an actuator disk, different zones can be defined: section (1) refers to the upstream, section (2) just before the propeller, section (3) immediately after the propeller, and section (4) refers to the downstream. The distance between (2) and (3) is assumed to be infinitesimal. So what happens is that the flow accelerates from section (1), characterized by V_1 and P_1, with an area A_1, to section (4) where we have V_4, P_4, and A_4. As defined by the actuator disk assumptions, the pressure at (1) and (4) is constant and equal to atmospheric pressure. The pressure change occurs between sections (3) and (4), that is, across the disk. Regarding velocity, it can be stated that $V_2 = V_3$, and V_2 can be written

as $V_2 = V_1(1+a)$; from this, the velocity increment through the disk $aV_1 = V_2 - V_1$ is derived, and the parameter a can be defined as the *axial inflow factor*. Similarly, it can be written that $V_4 = V_1(1+b)$, from which $bV_1 = V_4 - V_1$ is the other velocity increment, and the factor b is defined as the *slipstream factor*. Summarizing, we obtain the following:

$$a = \frac{V_2 - V_1}{V_1} \tag{2.1}$$

$$b = \frac{V_4 - V_1}{V_1} \tag{2.2}$$

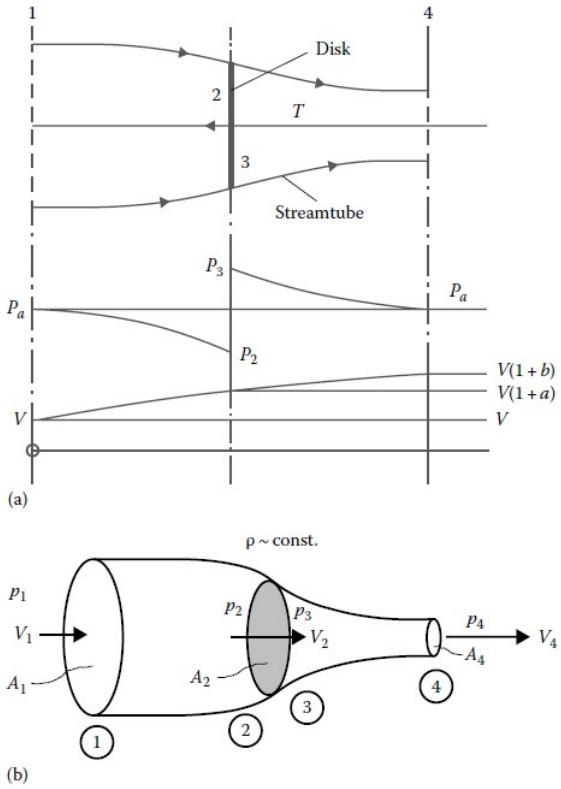

Figure 2.3: Actuator disk theory
[1]

First of all, thrust is analyzed

$$T = \dot{m}(V_4 - V_1) = A(P_3 - P_2) \tag{2.3}$$

Now we set $V = V1$ and knowing that $V_4 = V_1(1+b)$, we have

$$T = \dot{m}[V(1+b) - V] = \dot{m}Vb = AdP \tag{2.4}$$

$$\dot{m} = \rho A V_2 = \rho A V(1+a) \tag{2.5}$$

and thus, the thrust results

$$T = \rho A V^2 (1+a) b = A dP = A(P_3 - P_2) \tag{2.6}$$

from which the pressure jump

$$dP = \rho V^2 (1+a) b \tag{2.7}$$

At this point, we apply Bernoulli's theorem in the section between (1) and (2) and in the section between (3) and (4). It is worth noting that it is not possible to apply the theorem between (3) and (4) because the actuator disk does work in that section (there is a pressure change).

$$P_a + \frac{1}{2}\rho V^2 = P_2 + \frac{1}{2}\rho V^2 (1+a)^2 \tag{2.8}$$

$$P_3 + \frac{1}{2}\rho V^2 (1+a)^2 = P_a + \frac{1}{2}\rho V^2 (1+b)^2 \tag{2.9}$$

So the pressure difference results

$$dP = \rho V^2 b (1 + b/2) \tag{2.10}$$

In conclusion, from equation (2.7) and equation (2.10), one can derive the following relationship between a and b.

$$a = \frac{b}{2} \quad \text{or} \quad b = 2a \tag{2.11}$$

And it can finally be demonstrated, from equations (2.1) and (2.2), that

$$V_2 = \frac{V_1 + V_4}{2} \tag{2.12}$$

So if $V_1 = 0$, then $V_4 = 2V_2$. Therefore, by applying Bernoulli's theorem, it can be concluded that the fluid accelerates halfway between 1 and 2 and halfway between 3 and 4 at any velocity, even zero. To summarize briefly what actually happens, the actuator disk sucks in the air ahead (accelerating it decreases its pressure), then there is a pressure jump, and the acceleration that occurs between 3 and 4 causes the flow to lose the pressure gained previously on the disk.

One can then derive a relationship between thrust, the inflow factor a, or the slipstream factor b starting from the (2.6)

$$T = \rho A V^2 (1+a) 2a = \rho A V^2 \left(1 + \frac{b}{2}\right) b \tag{2.13}$$

which is quadratic in a or b, and solutions can be obtained

$$a = -\frac{1}{2} \pm \sqrt{\left(\frac{1}{2}\right)^2 + \frac{T}{2\rho A V^2}} \tag{2.14}$$

$$b = -1 \pm \sqrt{1 + \frac{2T}{\rho A V^2}} \tag{2.15}$$

From equations (2.14) and (2.15), it can be written that $v = Va$ and $w = bV$, where v and w are respectively the induced velocity at the disk and downstream of the disk.

$$v = aV = -\frac{V}{2} \pm \sqrt{\left(\frac{V}{2}\right)^2 + \frac{T}{2\rho A}} \tag{2.16}$$

$$w = bV = -V \pm \sqrt{V^2 + \frac{2T}{\rho A}} \tag{2.17}$$

Note that if $V = 0$, then $v = \sqrt{\frac{T}{2\rho A}}$;

At this point, the propulsive efficiency (or equivalently, efficiency) is defined as the ratio between the power available for thrust and the power generated by the engine to rotate the shaft.

$$\eta_p = \frac{TV}{P} \tag{2.18}$$

where

$$TV = \rho A V^3 (1+a) b = \rho A V^3 (1+a)(2a) \tag{2.19}$$

The power P is given by

$$P = \frac{1}{2}\dot{m}[V^2(1+b)^2 - V^2] \tag{2.20}$$

$$P = \rho A V^3 (1+a)^2 (2a) \tag{2.21}$$

From the ratio of equations (2.19) and (2.21), one finally obtains the so-called Froude efficiency, which is clearly valid only for the actuator disk model and represents the maximum upper limit achievable by a propeller's efficiency.

$$\eta_f = \frac{1}{1+a} = \frac{V_1}{V_2} = \frac{V}{V+v} \tag{2.22}$$

At this point, one can define the power loading (defined as power per unit area) and the disc loading (defined as thrust per unit area) as follows:

$$\frac{P}{A} = \frac{T}{A} V_2 \propto \left(\frac{T}{A}\right)^{3/2} \tag{2.23}$$

From equation (2.23), it can be deduced that if one wants to increase thrust, the induced velocity must be increased. However, if the induced velocity is increased, the jet loss also increases, and if the jet loss increases, the power grows not linearly with thrust but increases following a factor of $3/2$. In practice, if thrust increases by a factor of 2, power increases by $2^{3/2}$. Therefore, theoretically, if the area tends to infinity, then P/A and T/A tend to zero, from which it is deduced that to decrease power, the area of the propeller should be increased significantly, as observed particularly in helicopters, which have very large propellers.
Finally, to conclude with the actuator disk theory, the dimensionless parameters introduced in Chapter 1 are reported for completeness and convenience

1. Thrust coefficient
$$C_t = \frac{T}{\rho n^2 D^4}$$
2. Torque coefficient
$$C_q = \frac{Q}{\rho n^2 D^5}$$
3. Power coefficient
$$C_p = \frac{P}{\rho n^3 D^5} = \frac{2\pi n Q}{\rho n^3 D^5} = 2\pi C_q$$

4. Advance ratio
$$J = \frac{V}{nD}$$
5. Efficiency (or propulsive performance)
$$E = \frac{JC_t}{C_p}$$

From equation (2.23), the following relation comparing dimensionlessly power and thrust can be derived:

$$C_p = C_t^{\frac{3}{2}} \tag{2.24}$$

It is observed that if the propeller is loaded more, the efficiency decreases because the C_p grows faster than the C_t. On the other hand, if the advance ratio is increased, it is evident that the efficiency increases. In practice, the actuator disk theory states that the maximum efficiency of the propeller occurs when the propeller does not generate thrust, i.e., when the pitch angle β of the propeller is such that the angle of attack α equals the angle of zero lift.
The first three dimensionless parameters depend on the geometry, pitch, and area of the blades. What ultimately matters is the ratio between the physical area of the blades and the area of the propeller disc, called the blade solidity σ_R. If the blade solidity increases, C_T also increases; however, as mentioned earlier, if C_T increases, C_P increases even more, resulting in greater thrust but requiring more power.

$$\sigma_R = \frac{Bc}{\pi r} \tag{2.25}$$

With B being the number of blades, c being the chord of the blade, and r being the radius of the blade.

2.2.2 Blade element theory

Another theory of the propeller is the blade element theory, which involves considering each blade and evaluating the forces acting on each of them. What is interesting to do is a force balance based on the following image:

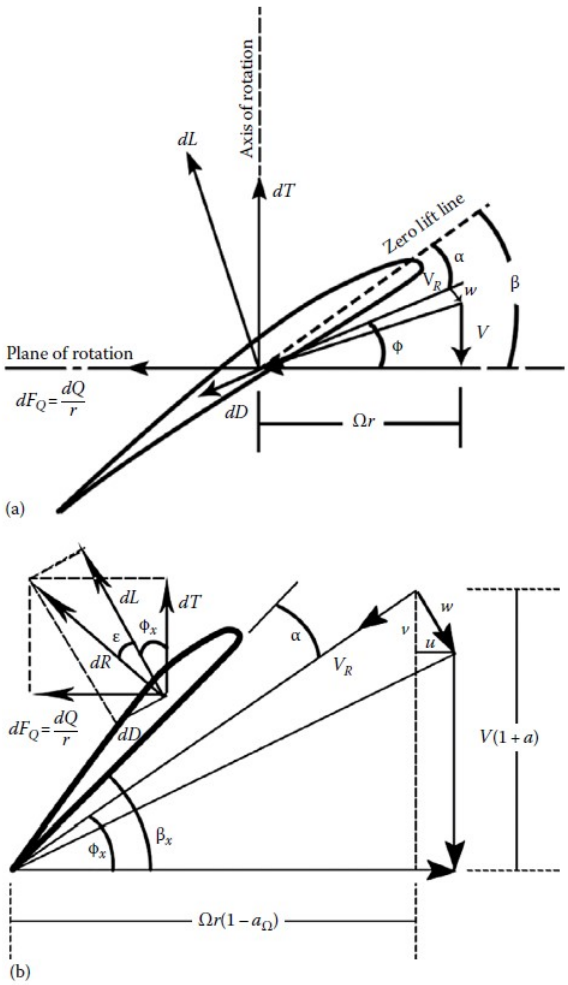

Figure 2.4: Blade element theory
[1]

$$\delta T = \delta L \cos\phi - \delta D \sin\phi = (l\cos\phi - d\sin\phi)\delta r \tag{2.26}$$

$$\frac{\delta Q}{r} = \delta L \sin\phi + \delta D \cos\phi = (l\sin\phi + d\cos\phi)\delta r \tag{2.27}$$

This is done to determine the torque Q and the thrust T. It is worth noting that the whole calculation is done considering a blade section. The idea is to find the lift per unit length l and the drag per unit length d for each blade section and then integrate equations (2.26) and (2.27) along r (starting from $r = 0$ and ending at $r = r_{tip}$).
For an airfoil profile, one can then express the lift coefficient and the drag coefficient for a blade section as follows:

$$C_l = \frac{l}{1/2\rho V_R^2 c} \tag{2.28}$$

$$C_d = \frac{d}{1/2\rho V_R^2 c} \tag{2.29}$$

in which C_l and C_d are known for an airfoil profile.
For the blade profiles, NACA profiles are commonly used (for example, NACA 4424 where the first digit indicates the camber, the second digit indicates the distance in percentage of camber from the leading edge, and the last two digits indicate the thickness percentage).

2.3 Ducted propeller

With the actuator disk theory, it is observed that in a free propeller, the flow is accelerated by the flow tube due to a pressure gradient.
In a ducted propeller, however, there is a propeller inside a duct where the velocity and pressure are constant; flow acceleration occurs in front of the duct, with a decrease in pressure before entering it.
It is now useful to make a comparison between a ducted propeller and a free propeller:

- For the ducted propeller: it is assumed that $V_4 = V_2$ with V_4 being the exit velocity and V_2 the velocity at mid-span between entrance and exit. The thrust T is fixed because $T = dPA$, but both pressure and area are known; in fact, $T = \dot{m}V_2$ and thus $V_2 = \sqrt{T/\rho A}$.
- For the free propeller: it is assumed that $V_4 = 2V_2$; knowing that $T = \dot{m}2V_2$ and recalling that $\dot{m} = \rho A V_2$, we obtain $V_2 = \sqrt{T/2\rho A}$.

Doing the calculations, it can be found that V_2 for a ducted propeller is 41% larger than for the free propeller, and since velocity and flow rate are related, the flow rate will also be 41% larger. This implies that at the same thrust, the free propeller is handling less flow rate, but it accelerates it by a certain amount halfway through the flow tube and doubles it at the end it. The ducted propeller, on the other hand, accelerates 41% of the air halfway through the duct, but then does not accelerate it further.
All of this has consequences in the calculation of power:

$$P = \frac{1}{2}\dot{m}V_2 = \frac{1}{2}\frac{T^{3/2}}{\sqrt{\rho A}} \tag{2.30}$$

$$P = \frac{1}{2}\dot{m}(2V_2)^2 = \frac{1}{\sqrt{2}}\frac{T^{3/2}}{\sqrt{\rho A}} \tag{2.31}$$

From equation (2.30) for the ducted propeller and equation (2.31) for the free propeller, it is realized that the power of the ducted propeller is 29% smaller than that of the free propeller.
Therefore, the higher the disc loading, the more advantageous it is to use a shroud, approaching turbofan-type propellers. The shroud is used to minimize the pressure gradient generated due to the increase in disc loading, but of course, the presence of such a shroud generates drag.

2.4 Propeller design

2.4.1 General characteristics

After a brief overview of propeller theory, the discussion moves on to the subject of this study, the NASA SR-3 propeller. This section summarises the main geometric characteristics of the propeller required to generate the 3D model. The SR-3 blade was designed by NASA to operate under cruise conditions at M=0.8, J=3.06, Cp=1.86, and altitude h=10668 [m]. To best generate the propeller geometry, the data obtained from the NASA report [4] are being used, and the corresponding graphs are presented in the following page. In figure 2.5, the variation of the twist angle β, lift coefficient C_l, thickness-to-chord ratio t/b, and chord-to-diameter ratio b/D is reported for each fractional radius of the blade. As for figure 2.6, it shows the variation of the sweep angle Δ also as a function of the fractional radius. The sweep angle is defined as the angle between the blade radius line (i.e. the stacking axis) and the line locally tangent to the sweep line [9], as shown in figure 2.7. The construction of the blade geometry refers to the manufacture sweep. Figure 2.5 shows that NASA uses two families of NACA profiles for blade construction. For the root section of the blade (from the root to $r/R = 0.37$), NACA series 65 profiles have been selected, characterized by a high t/b ratio, whose purpose is more structural than aerodynamic. The situation is different starting from $r/R = 0.53$ up to the tip, where NACA series 16 profiles are used, which have a significantly reduced t/b ratio and a very sharp leading edge to better adapt to transonic and supersonic phenomena. The region where $0.37 < r/R < 0.57$ is a transition zone where NACA family profiles is not used, but the reports [6] do not specify how the "transition" between the profiles before and after this transition region occurs. These profiles are chosen for their high critical Mach number and their ability to have a higher range of "drag buckets". [1].
In the report, NASA stated that this geometry is chosen to achieve maximum efficiency and minimum noise under design conditions (as defined in the previous chapter). Generally speaking, it is worth noting that in terms of aerodynamic performance, the sweep distribution is useful for reducing the relative Mach number along the blade below the critical Mach number corresponding to each airfoil profile. However, the chosen sweep is based on an acoustic theory aimed at minimizing noise as much as possible, while maintaining an acceptable structural design [6].

[1] **N.B**: The "drag bucket" range can be defined as a small range of angles of attack where the aerodynamic resistance of the wing profile is minimal.

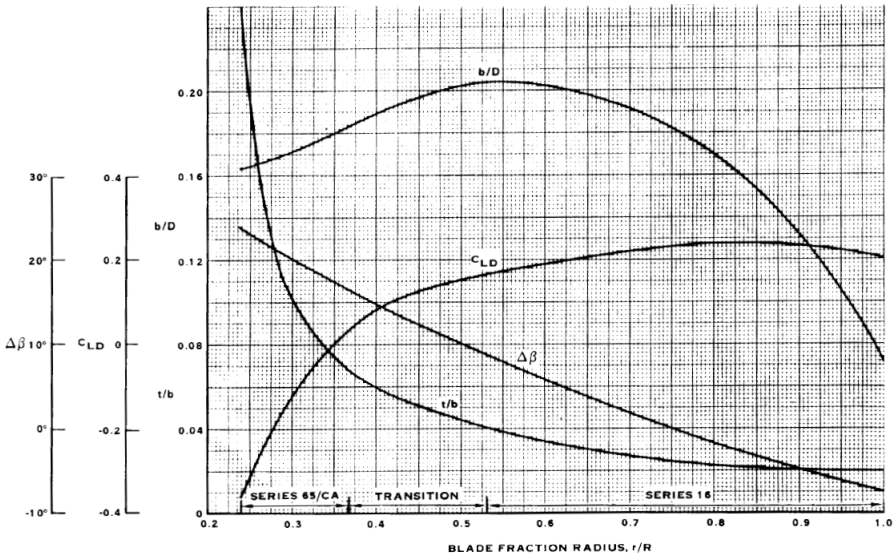

Figure 2.5: Characteristics of blade geometry
[4]

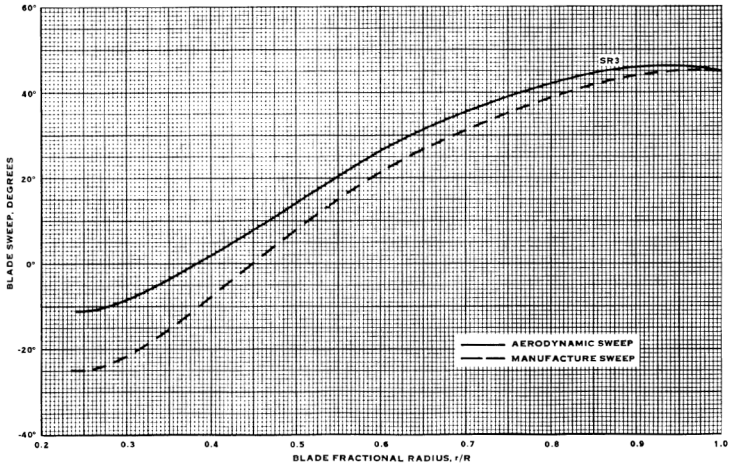

Figure 2.6: Blade sweep
[4]

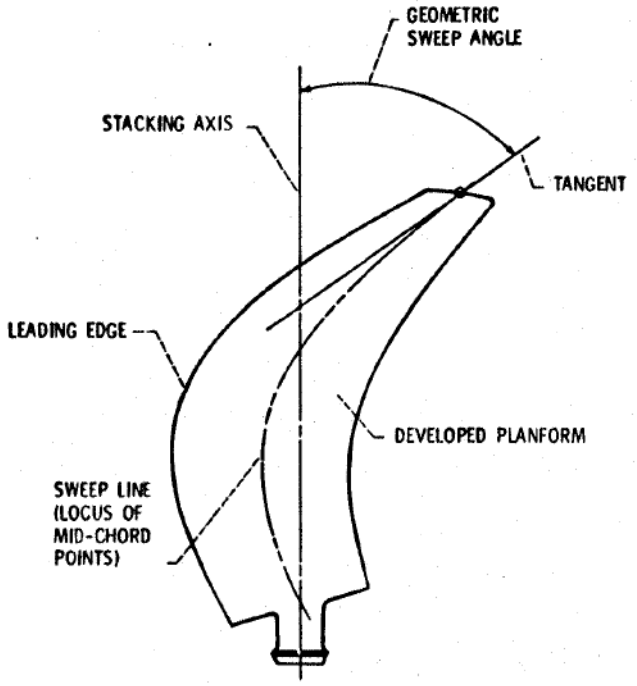

Figure 2.7: Sweep angle definition
[8]

At this point, it is possible to develop the 3D model of the blade, through several steps which are summarized and discussed in the following sections:

1. Generation of the 3D model within SolidWorks.
2. Script generation using the BladeModeler in the Ansys Workbench to extract the blade geometry from the CAD model.
3. Passing the blade from BladeGen to TurboGrid for mesh generation.

2.4.2 CAD design

The software used to generate the 3D model of the SR-3 propeller is SolidWorks [18]. Before model development, airfoil profiles used at various spans are derived based on the values of t/b, b/D, and Cl from figure 2.5. The profiles used are summarized in the table. 2.1

r/R	Airfoil section	r/R	Airfoil section
0.239	NACA 65A-424	0.6229	NACA 16-203
0.2492	NACA 65A-320	0.6746	NACA 16-203
0.2702	NACA 65A-214	0.7241	NACA 16-203
0.3014	NACA 65A-110	0.7731	NACA 16-202
0.3343	NACA 65A-008	0.8226	NACA 16-202
0.3666	NACA 65A-007	0.8743	NACA 16-202
0.5297	NACA 16-204	0.9228	NACA 16-202
0.5739	NACA 16-204	1	NACA 16-202

Table 2.1: Airfoil sections for SR-3 propeller

Once the profiles are identified, the points are exported from the open-source software OpenVSP [21] developed by NASA and imported into SolidWorks. Within the 3D modelling program, planes are positioned at the corresponding span for each profile. At this point, it is necessary to scale the profiles to the correct chord length (again based on figure 2.5) and stack them along an axis passing through the centroid of each, which is the pitch change axis. Once positioned, the profiles are assigned the corresponding twist angle and sweep angle, and in figures 2.11a and 2.11b, the final result can be observed. The sweep is assigned by sliding the profiles along the streamline passing through the reference span [6]. These streamlines are computed using Matlab [28], and a summary image is shown in the figure. 2.8.
It is important to underline that the tip profile is positioned according to the measurements indicated by the report. Referring to figure 2.9, the coordinates Z and Δ are specified by NASA, but how to derive them along the entire span of the propeller is not explicitly explained. Furthermore, it is stated that X varies with the pitch angle of the blade as a function of Δ and Z, but any relationship connecting them is not indicated. This leads to uncertainties regarding the final geometry of the propeller, particularly regarding the assignment of the sweep angle. The reports do not specify with respect to which plane such angle is measured, leading to incorrect values of Δ or Z. To assign the sweep, therefore, Z and Δ are relied upon as reference parameters. With the pitch angle set to $60.7°$, Δ and Z are assigned to the tip with the coordinate X derived as a consequence (fig 2.10). The position of the profile at the root is known instead, where the center of gravity (CG) is located exactly along the pitch change axis. For all other profiles, the sweep is applied based on images related to the developed planform of the blade present in the report [6]. Finally, a loft is performed between the profiles to obtain the final geometry. In the end, a blade is obtained with a root radius of $r_0 = 0.074m$ and a tip radius of $r_{tip} = 0.311m$.

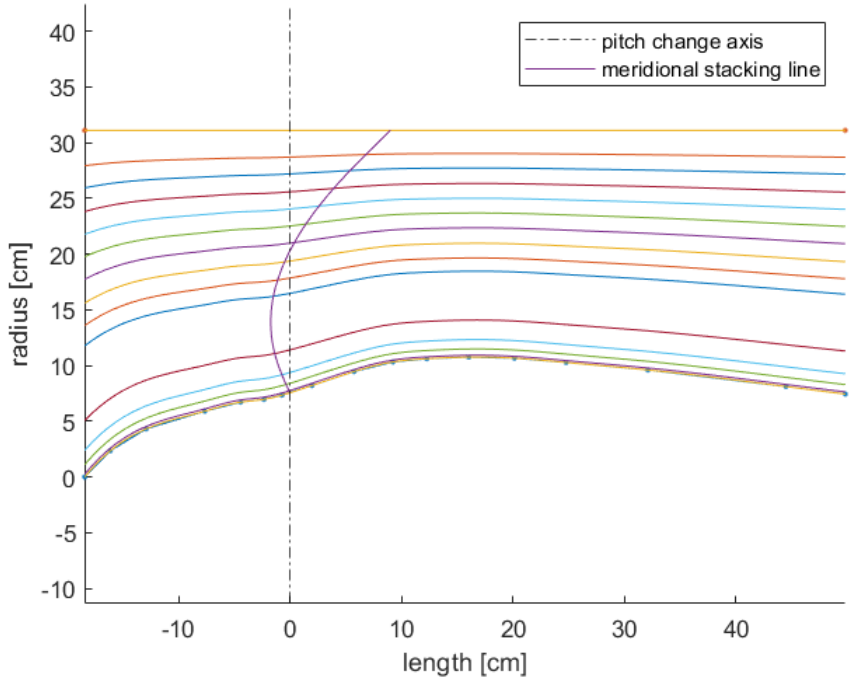

Figure 2.8: Streamlines

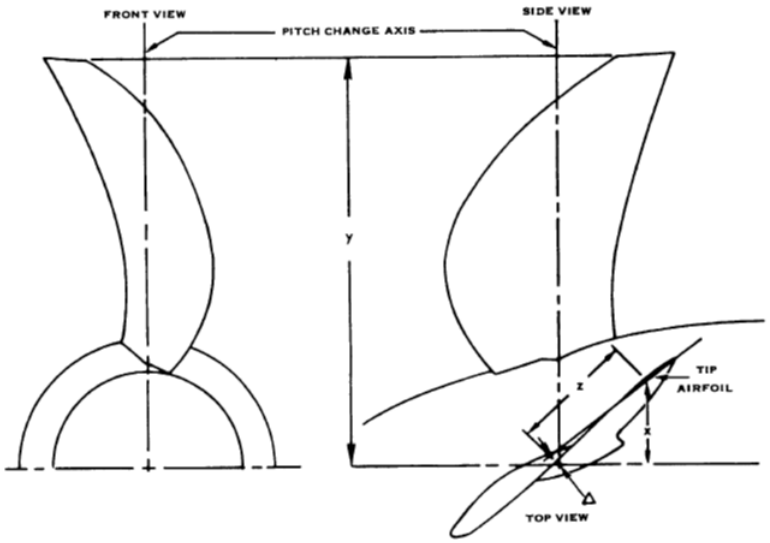

Figure 2.9: Three-view sketch of the SR-3 illustrating the position of the blade tip airfoil [6]

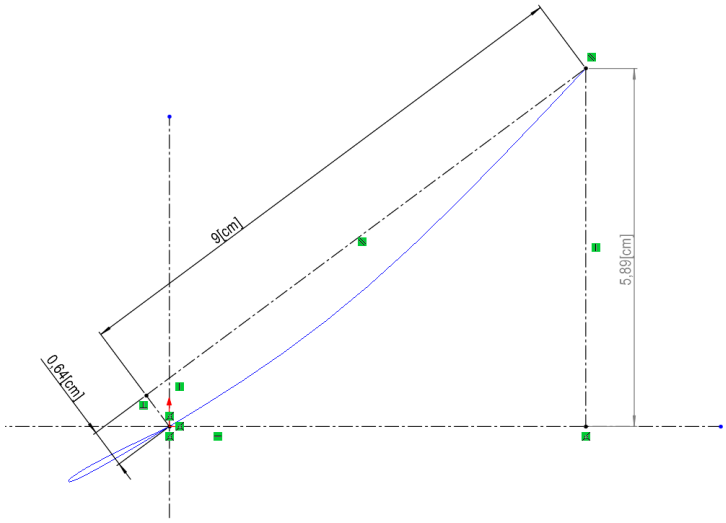

Figure 2.10: Tip CG location

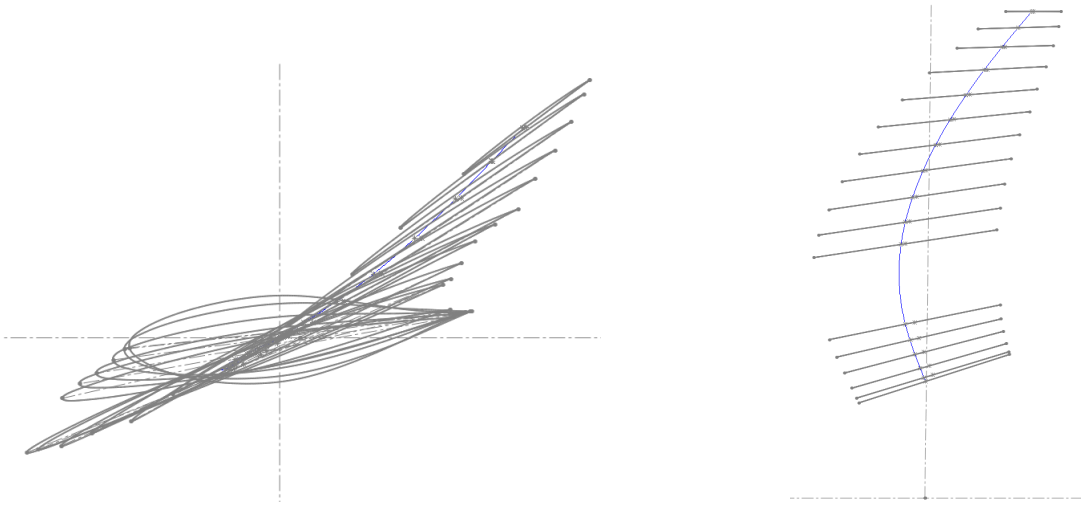

(a) Top view of stacking profiles

(b) Side view of stacking profiles

Figure 2.11: Top view and side view of stacking profiles

2.4.3 BladeModeler

Once the geometry is generated within SolidWorks, the process moves to Ansys DesignModeler to extract the blade geometry from the CAD model and ensure an automatic interface with TurboGrid. After designing the propeller in SolidWorks, a part of the cylindrical domain, highlighted in orange in figure 2.12 and 2.13 is added to enclose only one of the 8 blades.

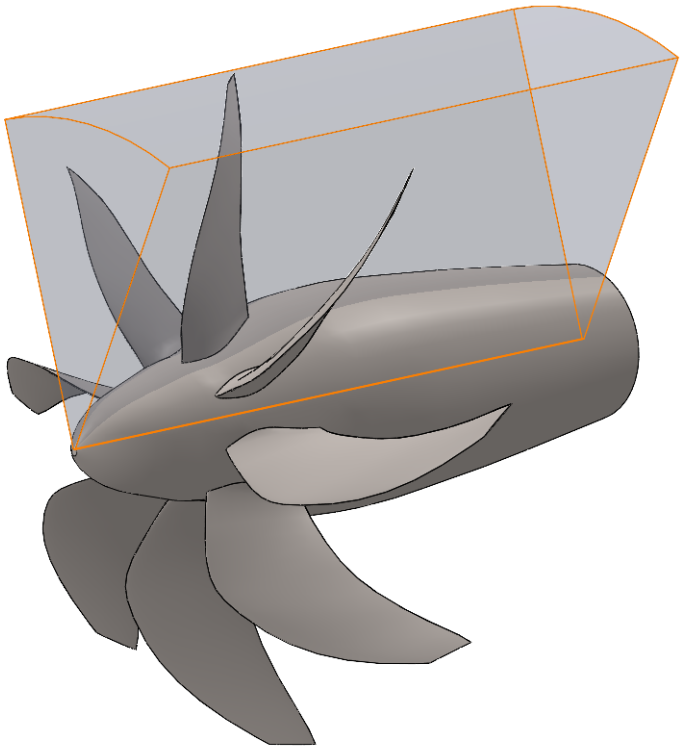

Figure 2.12: 3D view of the SR-3 propeller with a part of the cylindrical domain

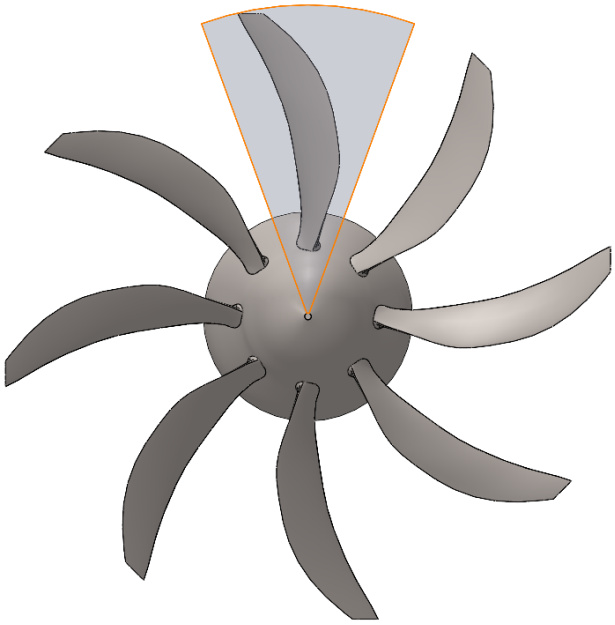

Figure 2.13: Front view of the SR-3 propeller with a part of the cylindrical domain

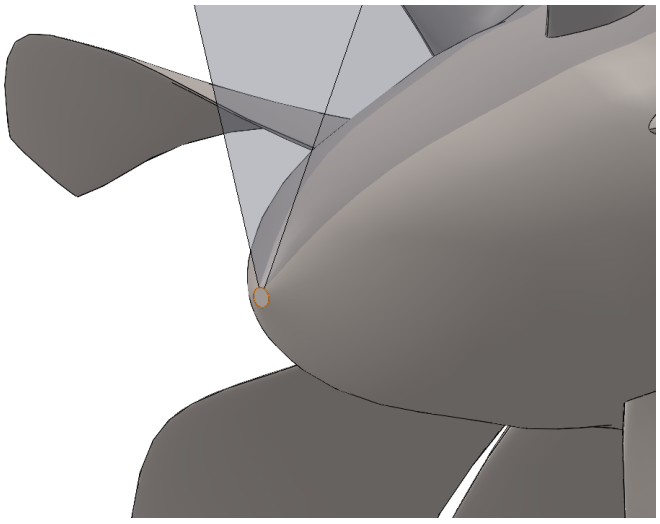

Figure 2.14: View of the gap near the rotation axis

2.5 Meshing

Once the geometry generation is complete, the mesh is generated on TurboGrid [20] for the blade, while another software is used for the external domain. The aim is to generate two domains: a rotating domain for the blade and an external stationary domain. The approach used to perform the simulations is the "Moving Reference Frame" (MRF). The size of the computational domain is chosen based on the report [7], and in figure 2.21 the final domain can be seen. The domain highlighted in green is the rotating domain of the blade, which is interfaced with the stationary one. For the stationary domain, the inlet and outlet are positioned respectively at a distance of $7D$ and $10D$ from the rotating domain of the propeller, and extends above the blade by a distance equal to $6D$. The height of the shroud of the rotating domain is instead placed at $0.65D$ from the hub surface. In figure 2.15, a sketch of the dimensions of the final domain is shown, with D representing the diameter of the propeller.

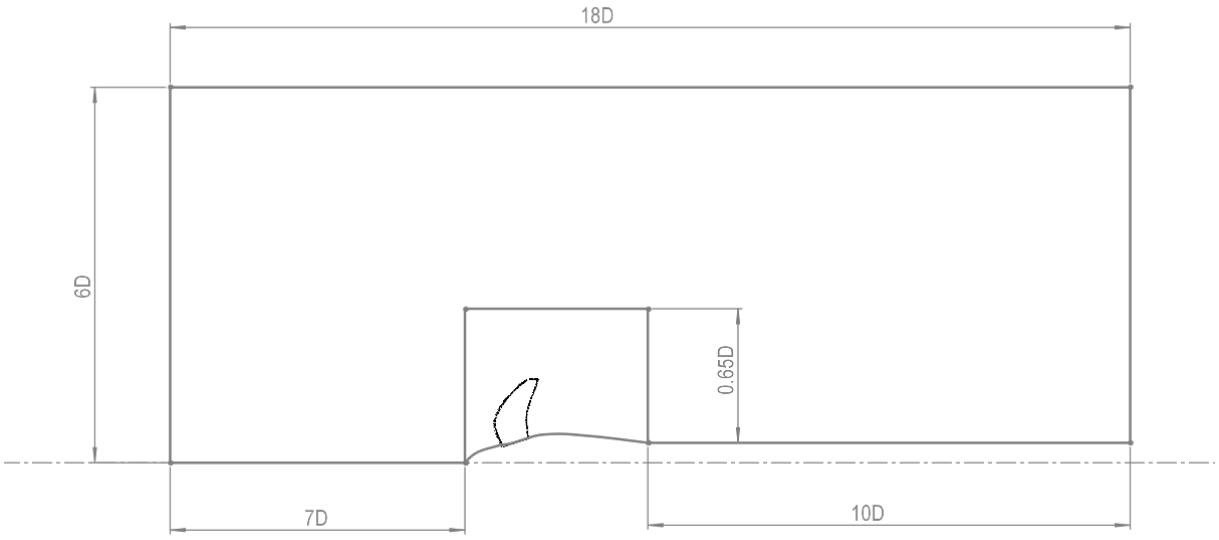

Figure 2.15: Domain size

2.5.1 Turbogrid Blade mesh

TurboGrid [20] is the software used to generate the blade mesh, as it is specifically designed to generate high quality structured meshes for turbomachinery. Once this has been clarified, the blade developed using BladeGen is imported into TurboGrid. The meshing process is then carried out. Four types of blade mesh are generated: the first one is very coarse with $4.121 * 10^5$ elements, the second one is coarse with $1.941 * 10^6$ elements and $y^+ = 50$, the third one has $3.071 * 10^6$ elements and $y^+ = 50$, and finally the finest one with $6.081 * 10^6$ elements and $y^+ = 1$. Inside TurboGrid, the y^+ is set by entering the Reynolds number and the desired y^+ value. In this case, the Reynolds number entered is calculated using the relation $Re = \rho V_\infty c/\nu$ based on the blade chord at the reference radius $R_{ref} = 0.75 r_t$. Below there is an image of the mesh performed on the blade (2.16) and on the hub (2.17).

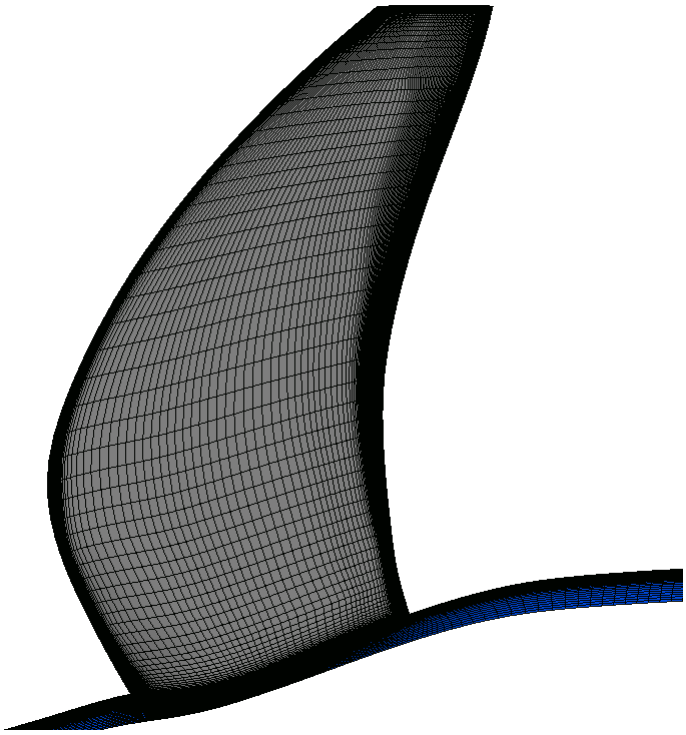

Figure 2.16: Blade mesh

Grid	Number of elements	y^+
Very coarse	$4.1210 * 10^5$	50
Coarse	$1.9410 * 10^6$	50
Medium	$3.071 * 10^6$	50
Fine	$6.0810 * 10^6$	1

Table 2.2: Blade passage number of elements

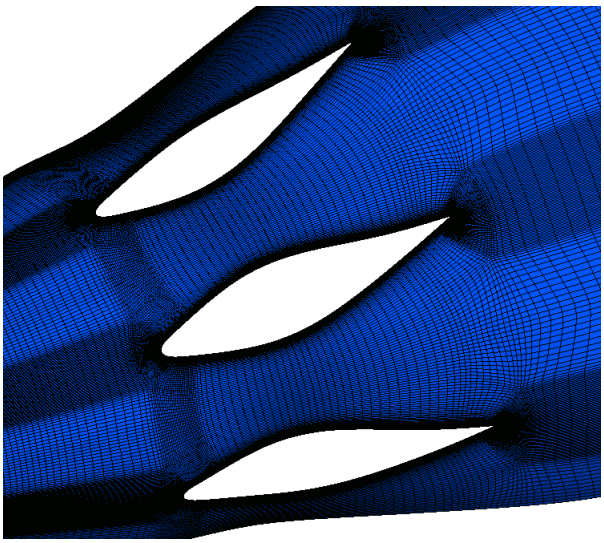

Figure 2.17: Hub mesh

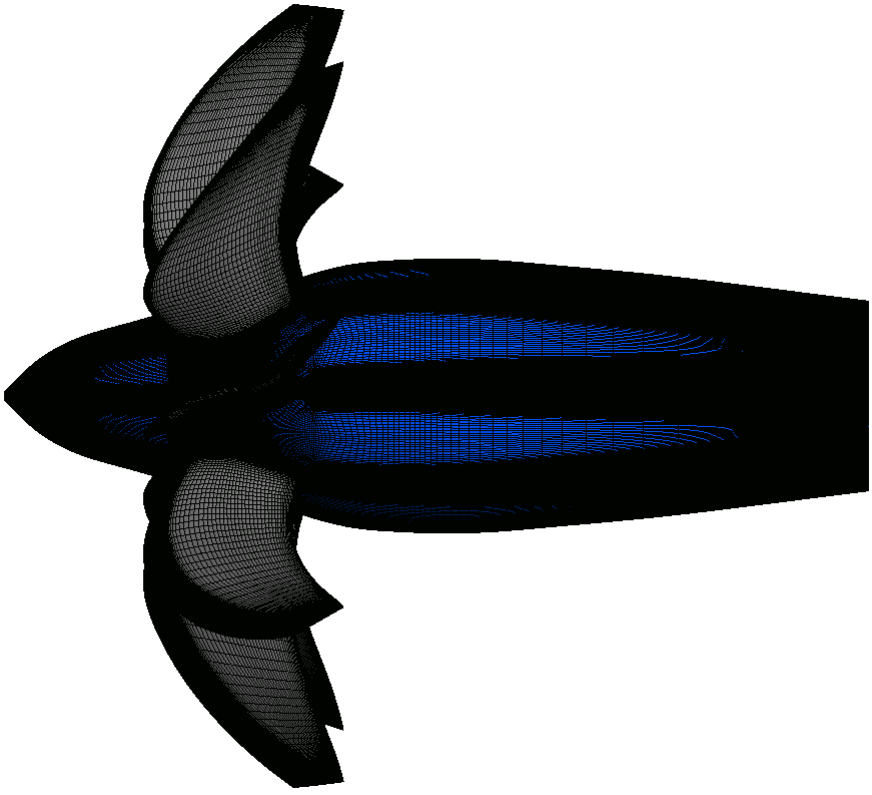

Figure 2.18: Propeller mesh

Below are two images showing the distribution of the wall y+ around the blade, respectively in the case of $y^+ = 50$ (figure 2.19) and $y^+ = 1$ (figure 2.20).

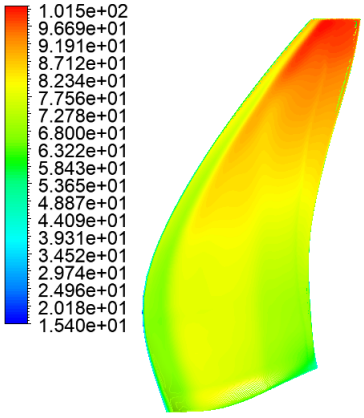

Figure 2.19: Wall y^+ distribution around the blade

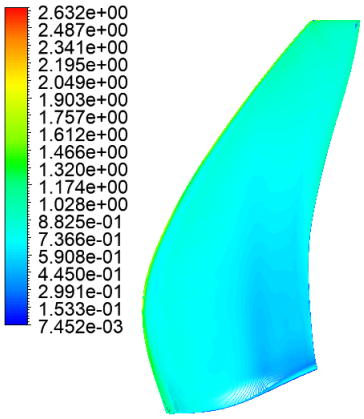

Figure 2.20: Wall y^+ distribution around the blade

2.5.2 External domain mesh

Once the mesh for the blade has been defined, the meshing process for the external domain is carried out, respecting the dimensions of the domain as shown in the previous figure 2.15. The final result is shown below. Similarly to the blade domain, three domains are generated for the external domain, with respective element counts of $1.751 * 10^6$, $2.449 * 10^6$, and $3.630 * 10^6$. As mentioned in the previous chapters, the shroud must be located at a height higher than what is allowed by TurboGrid, because the study involves an open propeller configuration where the shroud is not present in reality. Therefore, a small rotating domain (the green domain in fig 2.22) is generated along with the propeller to ensure that the shroud is sufficiently far from the propeller (specifically located at $0.65D$ as mentioned earlier).

Grid	Number of elements
Coarse	$1.751 * 10^6$
Medium	$2.449 * 10^6$
Fine	$3.630 * 10^6$

Table 2.3: External domain number of elements

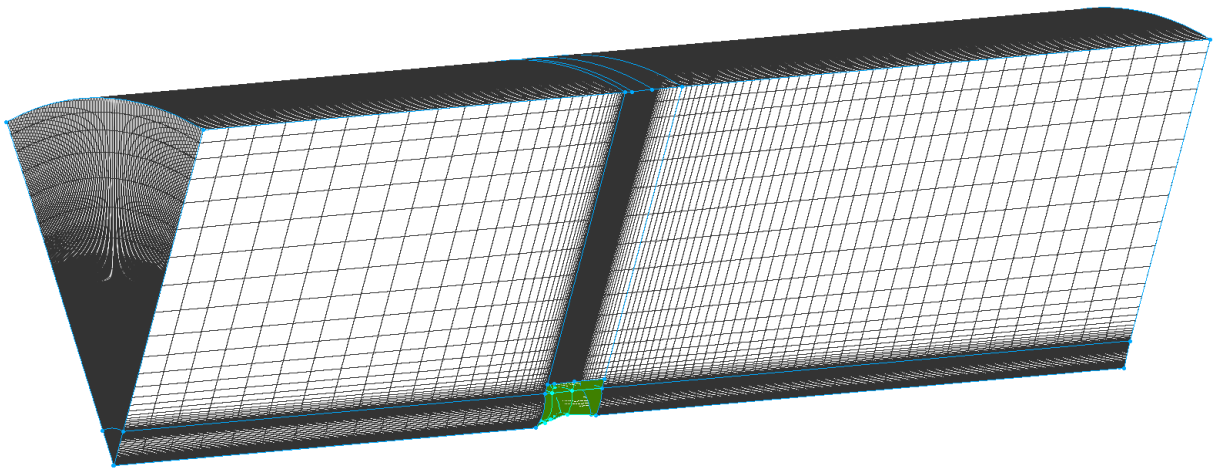

Figure 2.21: Mesh domain

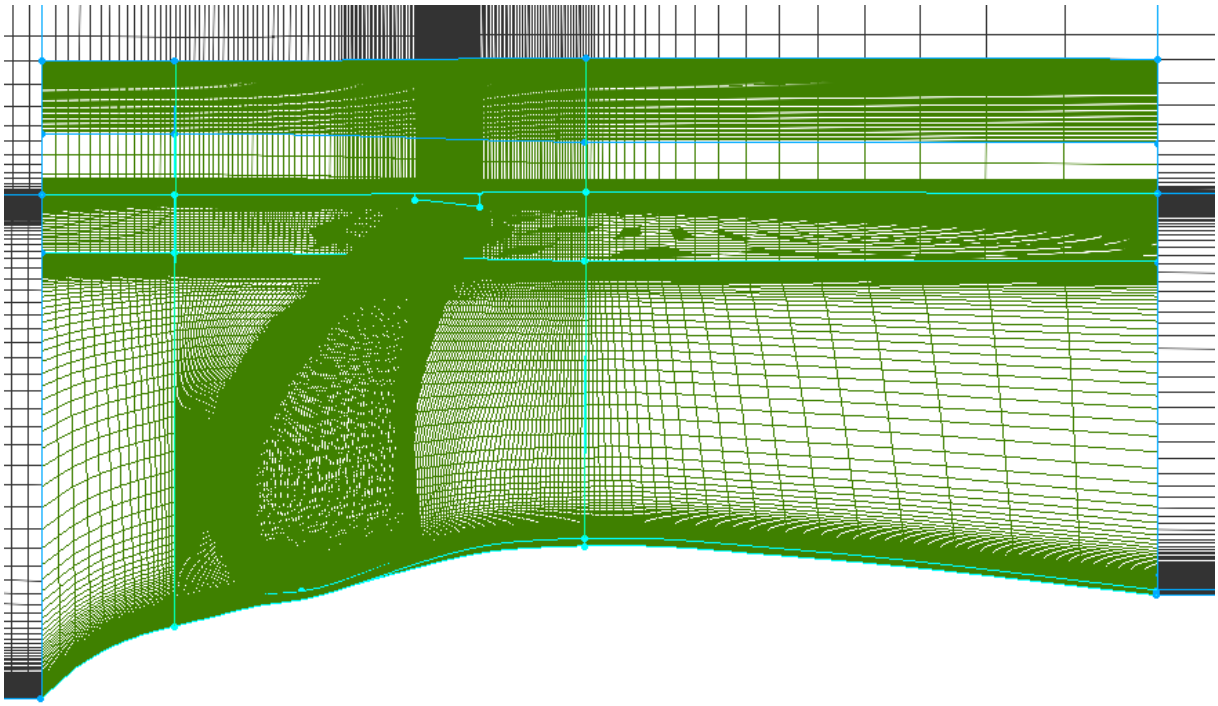

Figure 2.22: Detail of rotating domain

2.6 CFD analysis

2.6.1 CFD model

Once the mesh generation is complete, the CFD model can be developed on CFX-pre [19]. Here, the mesh generated by TurboGrid is imported, and then the mesh of the external domain is interfaced with it.
The mesh of the blade is divided into three parts called Ogive, Passage, and Outblock and the blade is located within the Passage. All three of these domains rotate at the same angular velocity, which varies depending on the desired advance ratio. The analyses performed are of steady-state type based on RANS equations and the turbulence model used is a $k-\omega\ SST$.
After defining the blade domain, the external domain is imported and interfaced with the rotating blade domain. Then, boundary conditions are assigned.
As mentioned in the "Meshing" paragraph, a Moving Reference Frame (MRF) model is analyzed. Therefore, regarding the interfaces, the "frozen rotor" option is assigned between each surface of the stationary mesh in contact with a surface of the rotating mesh. All surfaces in contact with each other, whether both rotating or both stationary, are still interfaced, but with a "none" type interface. Finally, the side walls of each domain are interfaced with a "rotational periodicity" type interface.
Once the interfaces are defined, boundary conditions are assigned to the external domain, where velocity inlet and static pressure outlet corresponding to the Mach number and flight altitudes, blade and hub are set as no-slip walls, while the upper outer wall is set as a free-slip wall. On the next page, there is a table (2.4) summarizing the boundary conditions used and a schematic image (2.23).

Location	Boundary condition
Inlet (1)	Velocity inlet
Outlet (3)	Static pressure outlet
Hub (6)	Moving wall
Blade	Moving wall
Hub-in (5)	Free slip wall
Hub-out (4)	Free slip wall
External wall (2)	Free slip wall

Table 2.4: Boundary conditions summary

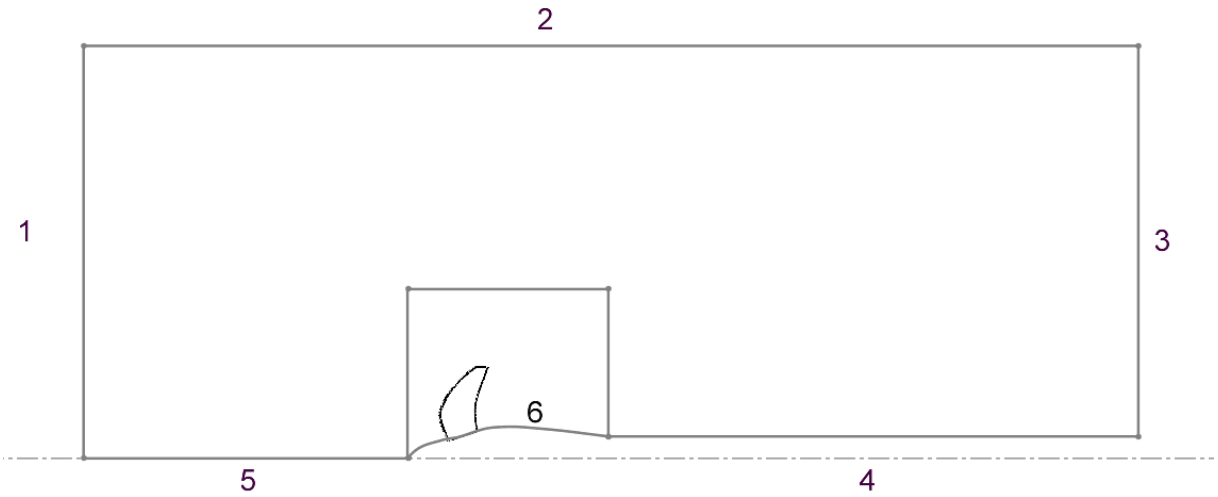

Figure 2.23: Boundary conditions

Finally, within the solver control, the advection scheme and turbulence numerics are set to high resolutions, and the compressibility control and high-speed numerics are activated. A physical timescale starting from $1/\omega$ is also used, then lowered during the simulation until finding the physical timescale that helps the simulation converge. Generally, lowering the physical timescale to $1/(160 * \omega)[s]$ has been enough to achieve convergence in simulations, setting a residual target of $1e - 6$ as the convergence criteria. In general, for a steady-state simulation, a high physical timescale allows for faster convergence, but the disadvantage is that it makes the solution unstable. Conversely, a low physical timescale will take longer to converge the simulation but in a more stable manner. Graphs related to simulation monitors are shown in figures 2.24, 2.26, 2.25 on the following pages.

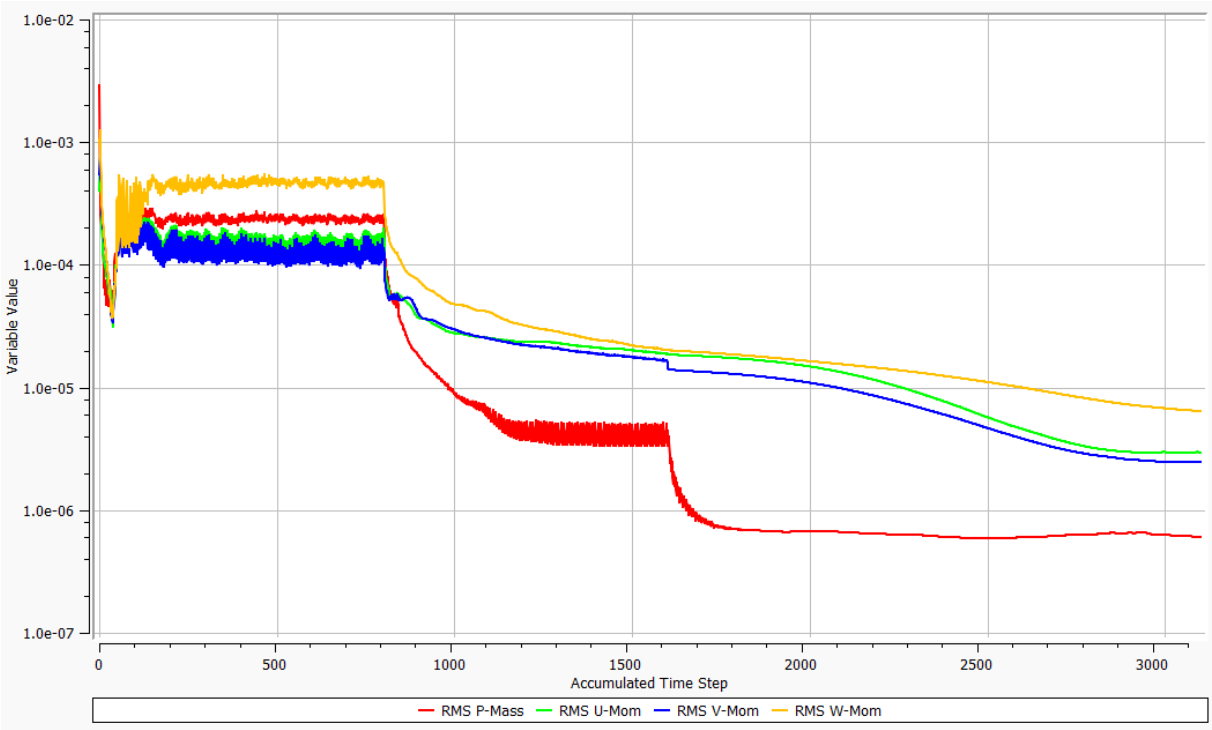

Figure 2.24: Residual monitor

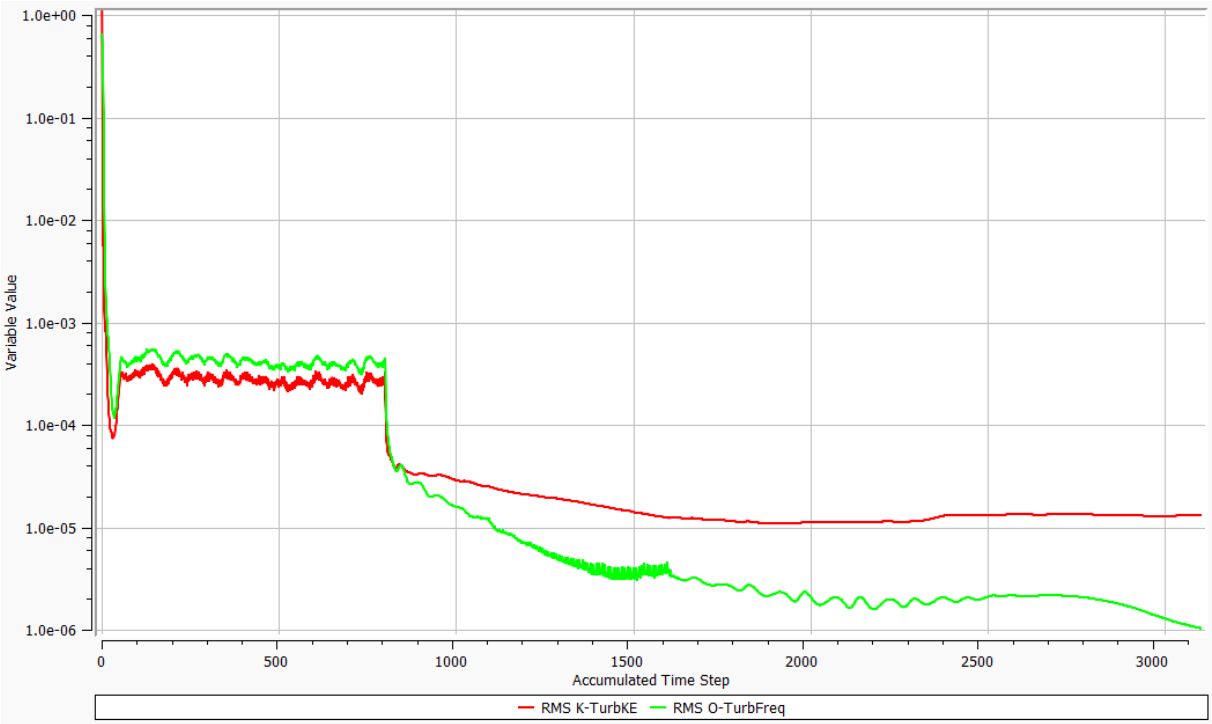

Figure 2.25: Turbulence monitor

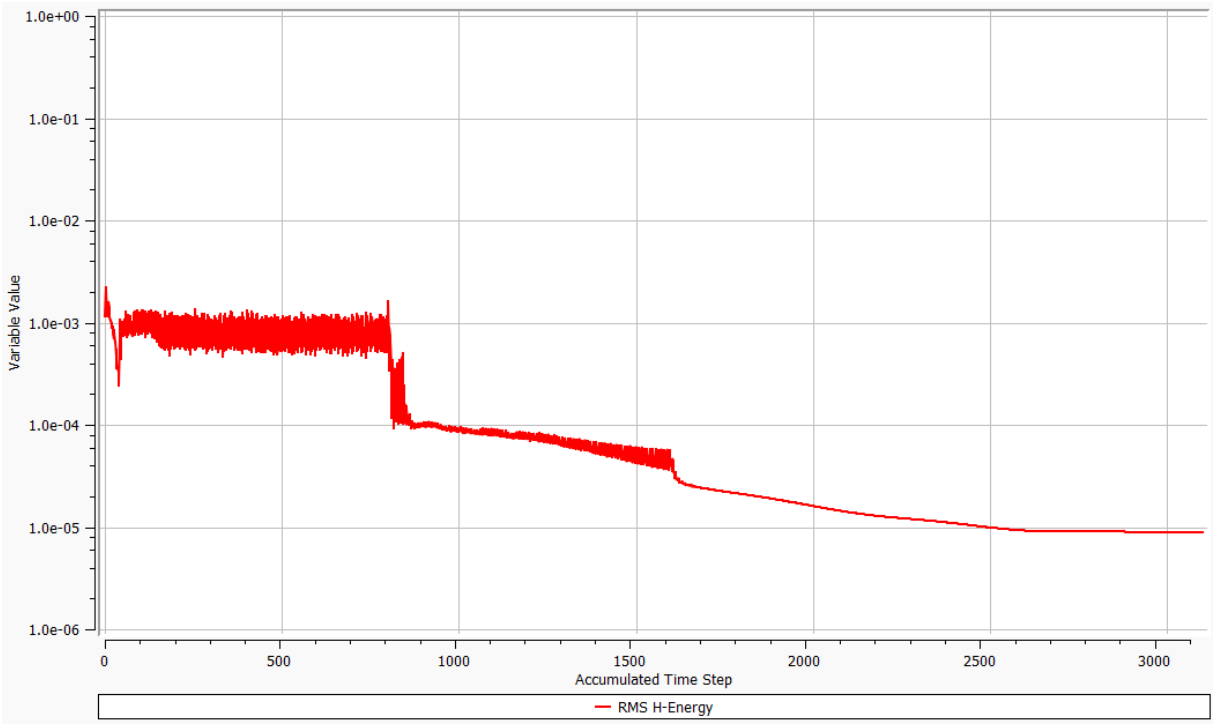

Figure 2.26: Energy monitor

In the graphs, the effect of the physical timescale can be observed. In the initial iterations, the solution oscillates without converging. From around iteration 800, the physical timescale is lowered by an order of magnitude, and at this point, the residuals noticeably decrease. At around iteration 1600, the physical timescale is lowered by another order of magnitude, resulting in further reductions in residuals and the solution tending to converge.

3 Results and Discussion

In this chapter, the results obtained from the simulations are presented and compared with the actual data acquired in the NASA laboratories to validate the CFD model developed. NASA conducts tests inside a 2.44 x 1.43m supersonic wind tunnel at various Mach numbers and pitch angles [6]. For these analyses, only the results of simulations with a pitch angle of 60.7° and a Mach number of 0.8 are reported.

3.1 Mesh sensitivity

The mesh sensitivity study, further explained later, is based on two approaches: first, the mesh is varied in the internal domain, then in the external domain, with the obtained graphs reported at advance ratios of J=2.9, J=3.06, and J=3.3.
In particular, a study on mesh sensitivity is conducted by varying only the blade mesh while keeping the mesh of the external domain fixed at $1.751 * 10^6$ elements. In figures 3.1 and 3.2, the trends of Cp and efficiency are shown as the mesh is refined. It can be observed that Cp remains approximately constant as the mesh is refined, while the efficiency undergoes some variations that, however, remain quite small, with the maximum being around 2% at an advance ratio of J=3.06 compared to the case with a denser mesh.
After refining the blade mesh, it is chosen to fix it at $4.821 * 10^6$ elements, and two further refinements of the external domain mesh are executed. The reason for not using the denser blade mesh is due to computational times and available computational resources, in addition to the fact that no substantial changes are observed from the sensitivity analyses. The results of the Cp and efficiency variation are reported in figures 3.3 and 3.4, where it can be observed that Cp undergoes a slight increase at all three advance ratios, leading to a slight decrease in efficiency (again, the maximum deviation is around 2%). Due to the computational cost required, further refinements of the external domain mesh are not possible. The results reported in the following paragraphs refer to the case with $5.4710 * 10^6$ elements.
In addition, a table (3.1) is provided with calculation times varying based on the number of mesh elements to perform 3100 iterations.

Grid	Number of elements	Calculation time [h]
Coarse	$4.821 * 10^6$	18.6
Medium	$5.520 * 10^6$	27.9
Fine	$6.708 * 10^6$	34.1

Table 3.1: Calculation time for different mesh size

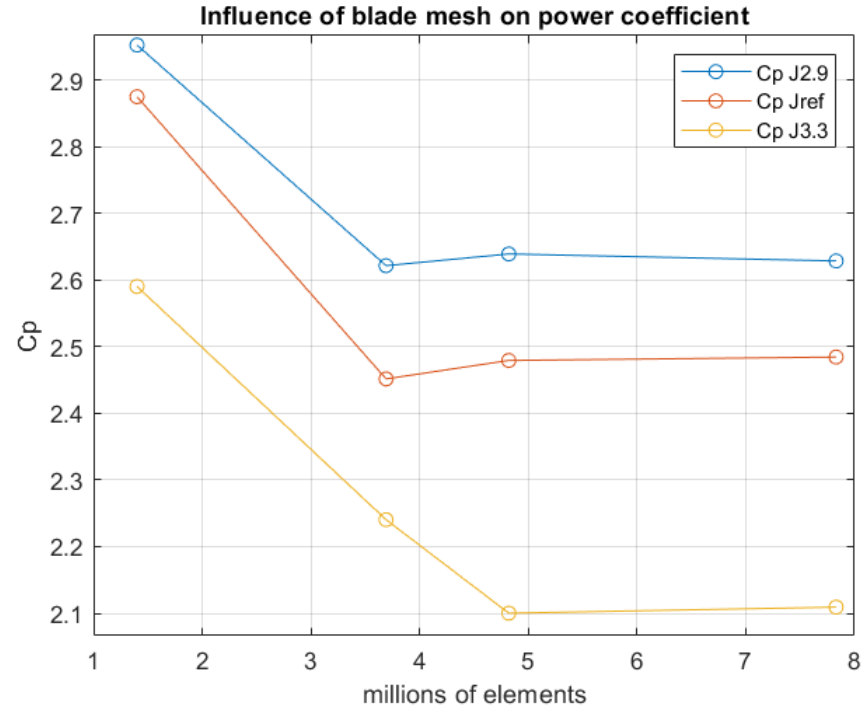

Figure 3.1: Blade mesh Cp sensitivity

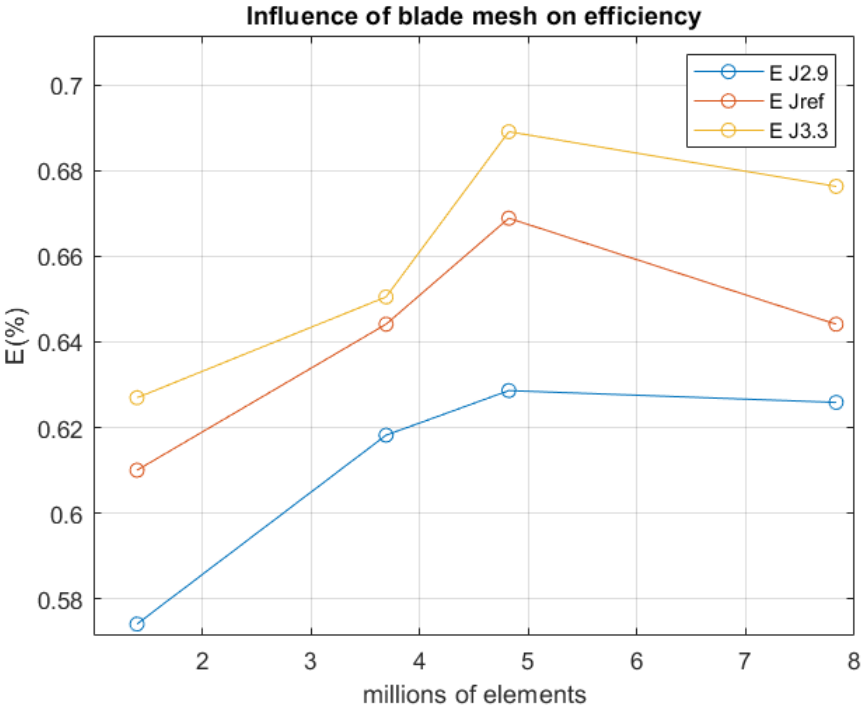

Figure 3.2: Blade mesh efficiency sensitivity

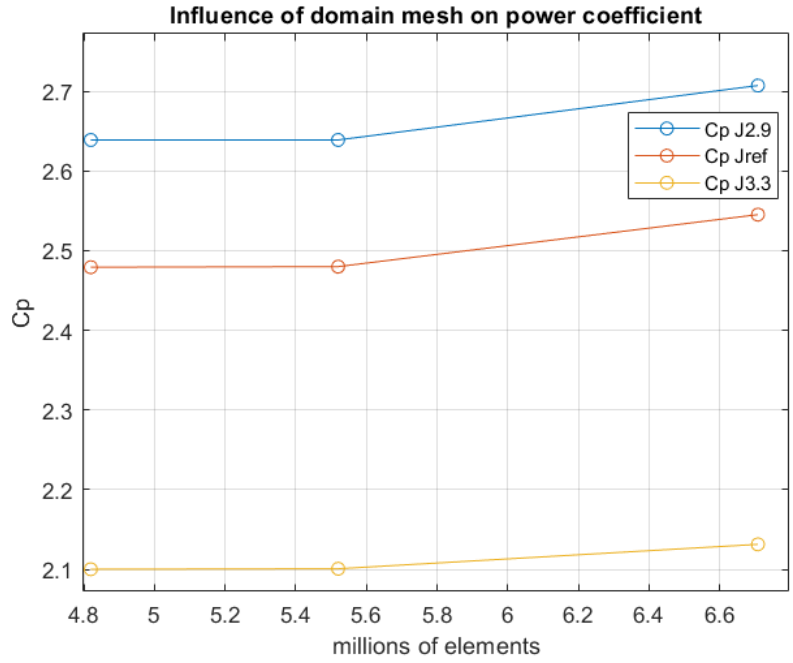

Figure 3.3: Domain mesh Cp sensitivity

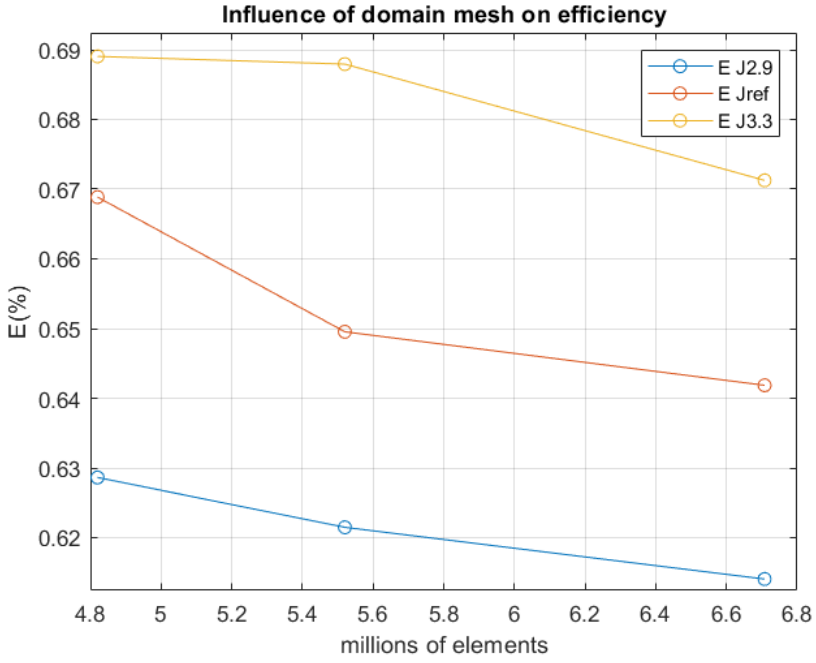

Figure 3.4: Domain mesh efficiency sensitivity

3.2 Performance data

On the next page, the graphs relating to the performance parameters of the propeller obtained from the CFD simulations are presented and compared with the actual values derived from the NASA wind tunnel tests.
In figure 3.5, the efficiency trend of the propeller at 60.7 degrees pitch obtained from the CFD simulations is represented. The maximum efficiency from the simulations occurs at an advance ratio of J=3.5 with a peak of 71%, while in the real case, the maximum achieved efficiency is 78.2%.
Such a discrepancy can be justified by considering the graph in figure 3.6 of the power coefficient, which is reported on the following page.
As mentioned in previous chapters, the SR-3 blade was designed by NASA to operate under cruise conditions at M=0.8, J=3.06, Cp=1.86, and altitude h=10668 [m]. Observing the graph in figure 3.6 of the power coefficient, it is noted that at small advance ratios, the CFD simulations overestimate the value of Cp, while as the advance ratio increases, this discrepancy reduces.
In the reports, NASA stated that at high loads (i.e., low advance ratios), the blade deforms significantly, increasing its diameter due to centrifugal loads and aeroelastic phenomena, but never specified the extent of this deformation. This deformation clearly has crucial effects, in the sense that in addition to the increase in diameter, as expressed by theories of aeroelasticity ([15]) a variation in the angle of incidence of the blade also occurs. Unfortunately, it is not possible to take this phenomenon into account in the CFD simulations as it is very complex and would require a much more in-depth study on its own.
Therefore, having overestimated the power coefficient and remembering that efficiency depends on the ratio between the thrust coefficient and the power coefficient ($E = J\frac{Ct}{Cp}$), it is easy to conclude why the efficiency is smaller than in the real case.
Regarding the values of torque and thrust of the propeller, NASA does not publish any data on their variation with respect to the advance ratio. However, the trends calculated by the CFD simulations are still reported in figure 3.7 and 3.8.

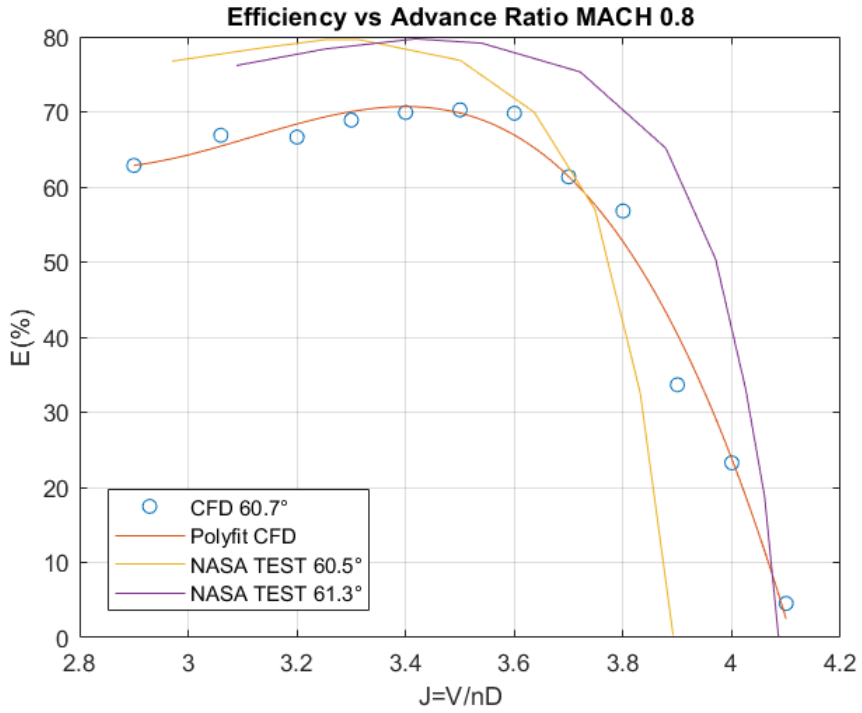

Figure 3.5: Efficiency vs Advance ratio M0.8

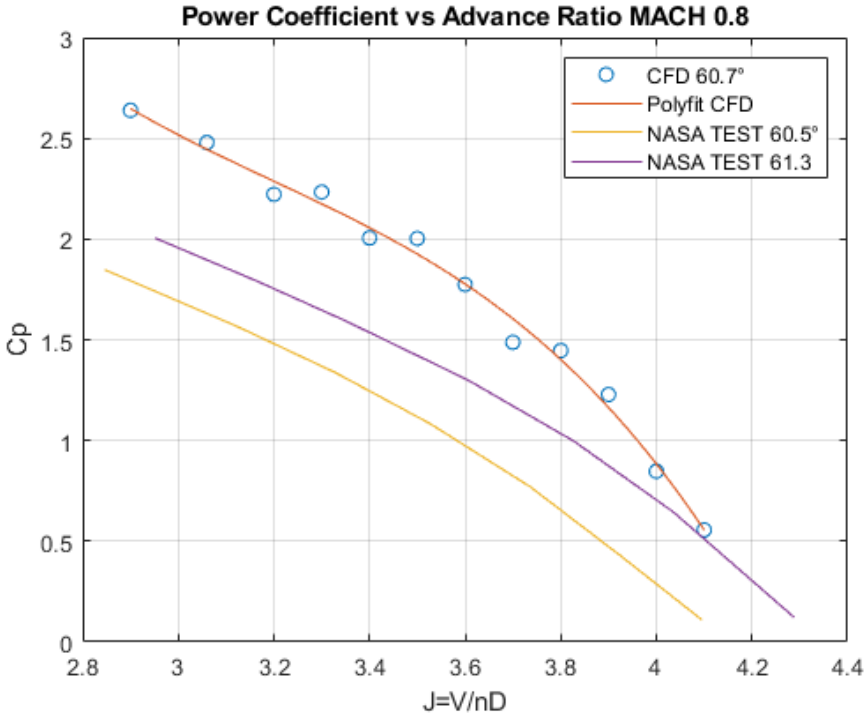

Figure 3.6: Power coefficient vs Advance ratio M0.8

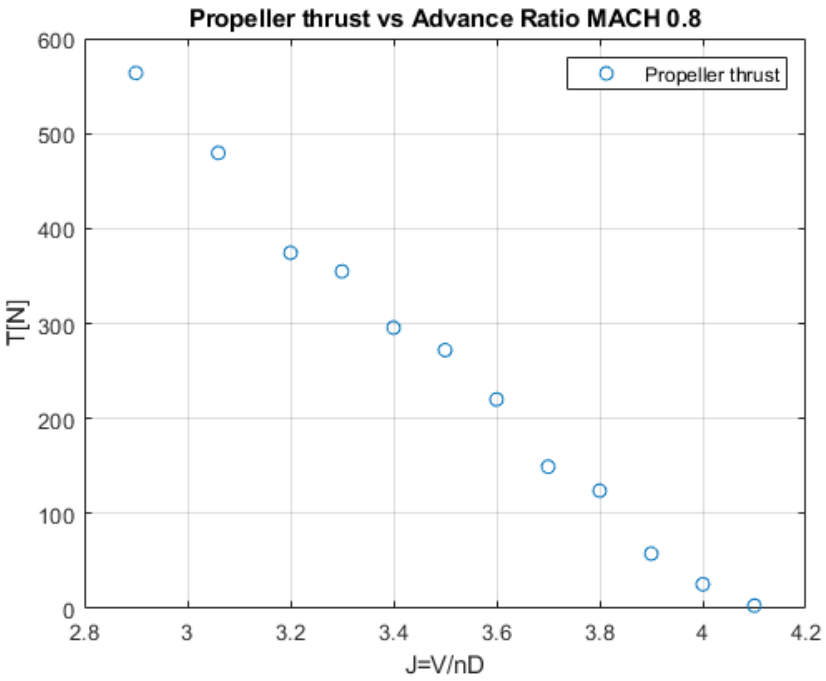

Figure 3.7: Propeller thrust

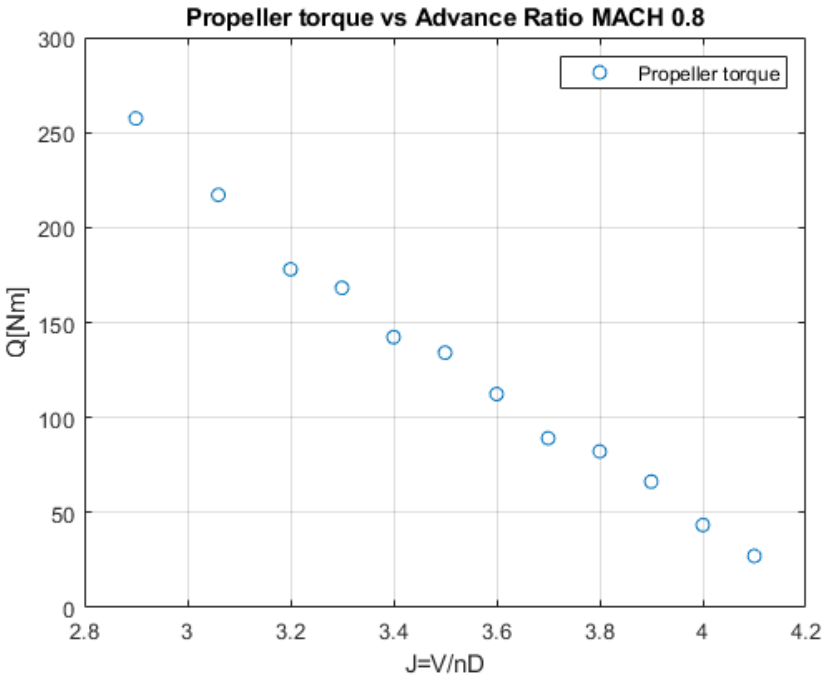

Figure 3.8: Propeller torque

Regarding the calculation method of the propeller thrust, the following formula is used:

$$dF = (P - P_0)\hat{n} + \tau\hat{n}dA \tag{3.1}$$

where dF is the force acting on a surface and is the sum of the pressure component and the viscous component. To evaluate the total thrust, it is therefore necessary to sum the forces acting along Z on all surfaces, i.e., on every element of the mesh of interest.
In this case, it is necessary to evaluate not only the thrust of the blade but also the drag of the hub to obtain the total net thrust of the propeller along the Z-axis.
The same applies to the calculation of the propeller torque, where the torque is evaluated vectorially using the following formula:

$$dQ = dF_xY - dF_yX \tag{3.2}$$

In this case as well, it is necessary to sum up the torque required to rotate each individual element of the mesh. To measure the net thrust of the propeller (T_{net}), NASA first conducted measurements of the drag generated by the shaft (ΔD_N) using a "dummy" shaft without the blade mounting locations. Then, this drag is subtracted from the apparent force (T_{app}) generated by the propeller (which is the force generated and measured without considering the mutual interaction between the blades and the shaft) [6].

$$T_{net} = T_{app} - \Delta D_N \tag{3.3}$$

$$T_{app} = FB - \sum PA_{int} + D_s \tag{3.4}$$

$$\Delta D_N = D_N - D_{NT} \tag{3.5}$$

$$D_N = \int (P - P_0)dA \tag{3.6}$$

In this "dummy" shaft, the spinner drag (D_s) and the nacelle pressure drag (D_{NT}) are measured. Concerning the spinner drag, it is directly measured using a force balance (FB), with a correction made for internal pressure forces ($\sum PA_{int}$). As for the nacelle pressure drag, it is measured by integrating the pressure inside orifices placed along longitudinal rows, as stated by [6]. Summary images are provided in figure 3.9 and 3.10.

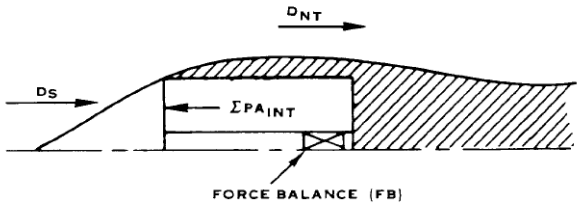

Figure 3.9: Hub without blades for drag measurements

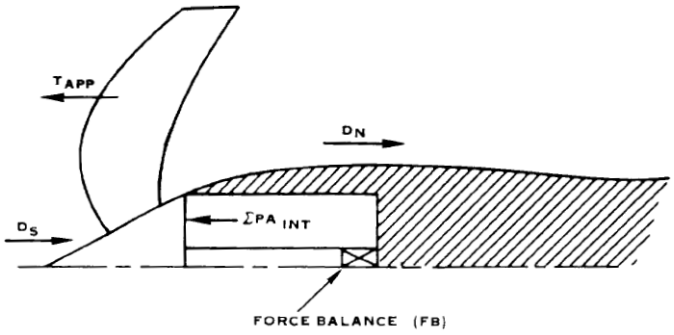

Figure 3.10: Propeller forces

Having clarified the discussion regarding the force evaluation method carried out in the NASA laboratories, below are some graphs relating to the axial velocity measured at the blade exit. Specifically, NASA positioned a laser velocimeter at x/R=0.89 (i.e., at the trailing edge of the blade tip) and respectively at spans s=0.35, s=0.65, s=1.03. In figures 3.11, 3.12, and 3.13, the comparison between the velocities obtained from the CFD analysis and the real case, as well as the theoretical case evaluated by NASA using the lifting line theory, is shown.
In the cases at spans s=0.35 and s=1.03, the velocity trend is almost consistent with the NASA measurements, while in the case at span s=0.65, the trend does not match the real case, but it more closely reproduce the theoretical case evaluated with the lifting line analysis. Furthermore, in the cases at spans s=0.65 and s=1.03, the velocity is slightly underestimated by the CFD simulations.

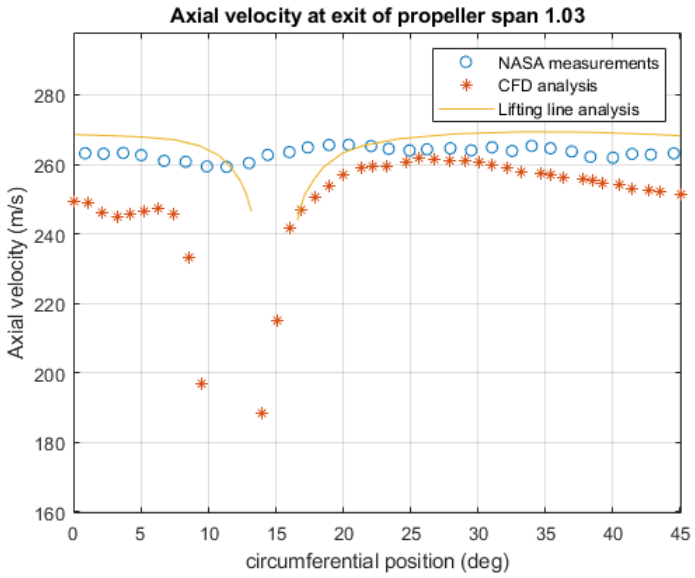

Figure 3.11: Axial velocity x/R=0.89 s=1.03

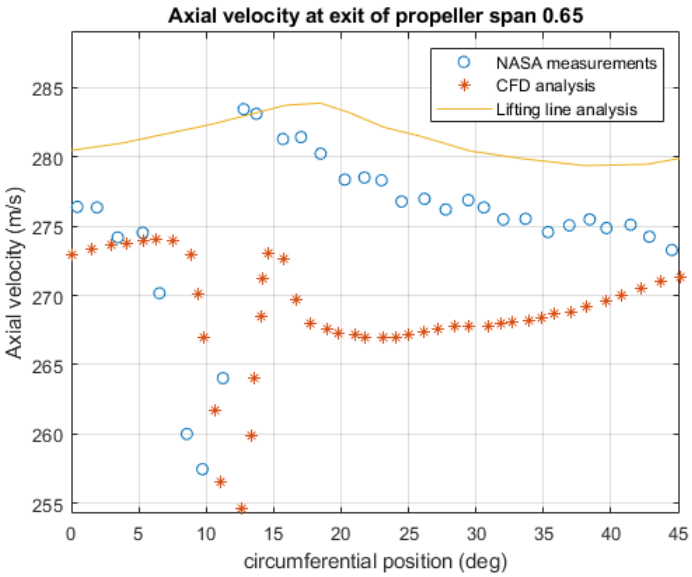

Figure 3.12: Axial velocity x/R=0.89 s=0.65

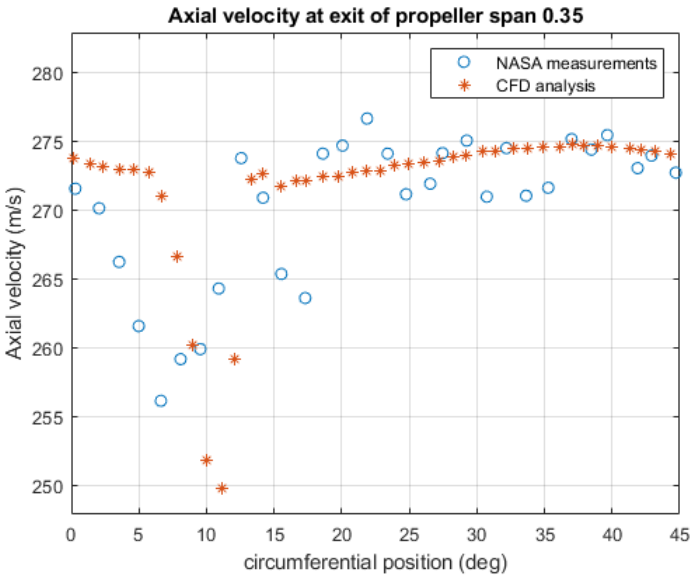

Figure 3.13: Axial velocity x/R=0.89 s=0.35

Some velocity and pressure images obtained from the CFD simulations are presented on the following pages. In figure 3.14a and 3.14b the trend of the Mach number and the distribution of streamlines at a span near the tip at J=3.06 are observed. In particular, it can be seen how the boundary layer tends to separate at the leading edge, then manages to reattach towards the trailing edge. Additionally, the shock-wave generated at the trailing edge can be observed, which, as also stated by NASA [6], is the cause of the high noise generated by this propeller.

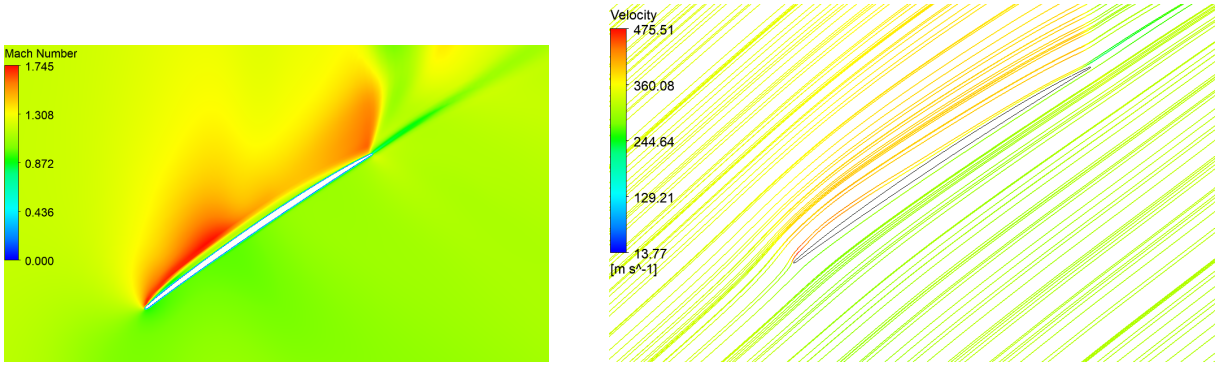

(a) Mach number near-tip

(b) Streamlines near-tip

Figure 3.14: Trend of the Mach number and streamlines around near-tip profile at M0.8 and J3.06

The image below 3.15 shows boundary layer separation at the blade tip, although in the NASA report this separation is not specified.. The causes of boundary layer separation can be twofold: firstly, the geometry may not be exactly identical to the real one due to the lack of some data to generate it optimally; secondly, the blade may deform under high loads, leading to a more or less pronounced variation in the angle of attack of the tip, which prevents boundary layer separation. At higher advance ratios, boundary layer separation no longer occurs, as observed in the figures 3.20a and 3.20b.

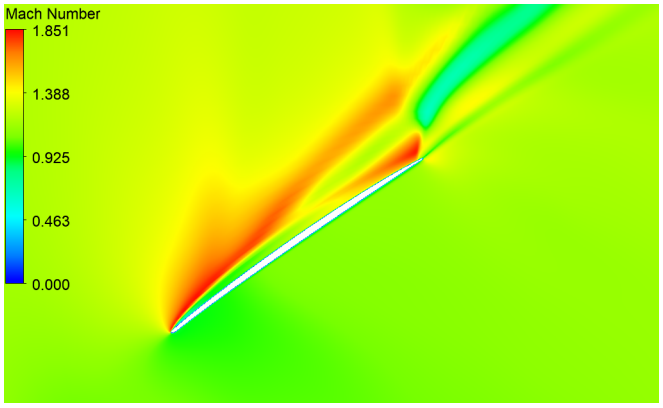

Figure 3.15: Boundary layer separation at the tip of the blade at M0.8 and J3.06

Images depicting velocity and streamlines around near-root profiles are shown (figures 3.16a, 3.16b), as well as mid-span profiles (figures 3.16c, 3.16d) in the case of J=3.06. The formation of a sonic leading-edge bubble can be observed in the near-root profile case, with the flow still remaining well attached to the profile as seen in figure 3.16b. In the mid-span case, the shock forms at the trailing edge, and up to that point, the flow remains well attached to the back of the profile. After the shock, the flow returns to being subsonic.

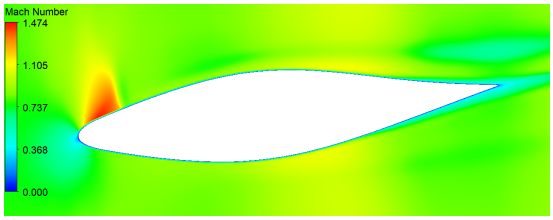

(a) Mach number near-root

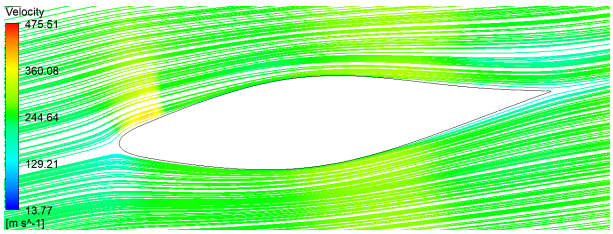

(b) Streamlines near-root

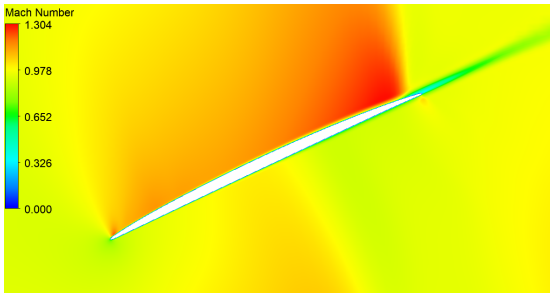

(c) Mach number mid-span

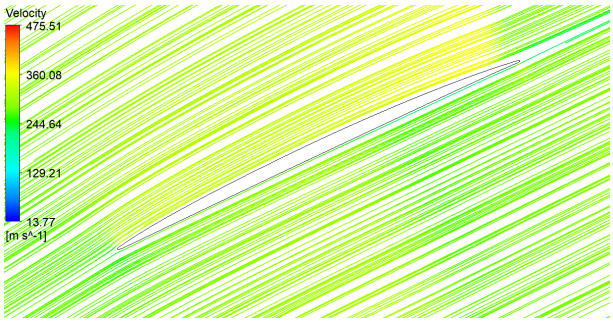

(d) Streamlines mid-span

Figure 3.16: Trend of the Mach number and streamlines around the profiles at low-span and mid-span at M0.8 and J3.06

To conclude this thesis, for completeness, some images related to the distribution of Mach number and streamline behavior around profiles at advance ratios J=2.9 and J=3.5 at different spans are reported. Again, in figure 3.17a the sonic bubble forming at the leading edge in the case of J=2.9 can be observed, with the streamlines 3.17b closely following the profile's edge. For J=3.5 in figures 3.17c and 3.17d, the same considerations as for J=2.9 apply. It can be seen that the speeds obtained around the profiles are higher at low advance ratios and vice versa. This is due to the fact that at low advance ratios the propeller turns faster. This speed difference is less noticeable at the root of the blade.

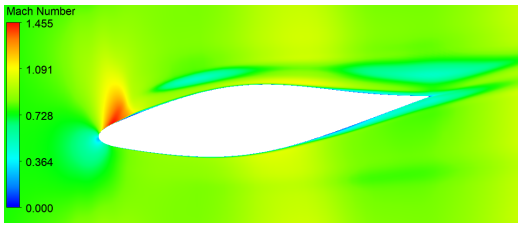

(a) Mach number trend near-root J2.9

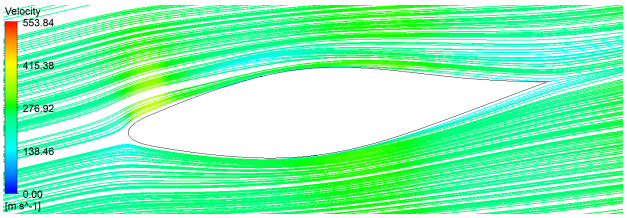

(b) Streamlines trend near-root J2.9

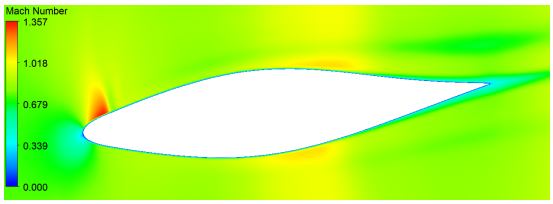

(c) Mach number trend near-root J3.5

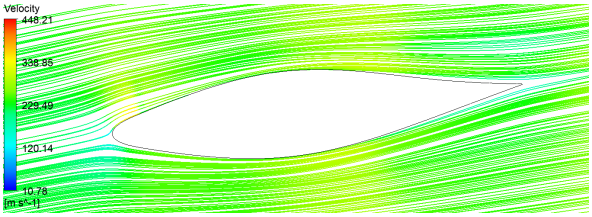

(d) Streamlines trend near-root J3.5

Figure 3.17: Trend of the Mach number and streamlines around the profiles near-root at M0.8, J2.9 and J3.5

Figures 3.18a, 3.18b for J=2.9 and 3.18c, 3.18d for J=3.5, show the distributions of Mach number and streamlines around the mid-span profiles of the blade are depicted. In both cases, the flow remains attached to the profile until the trailing edge, where a shock is generated.

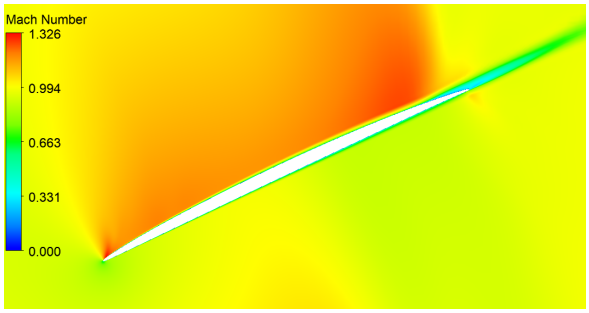

(a) Mach number trend mid-span J2.9

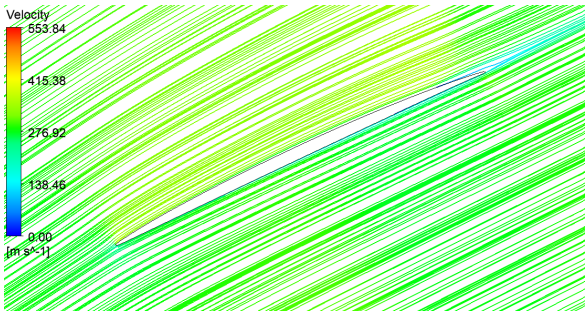

(b) Streamlines trend mid-span J2.9

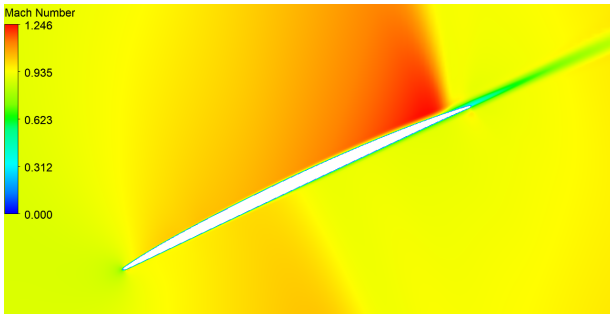

(c) Mach number trend mid-span J3.5

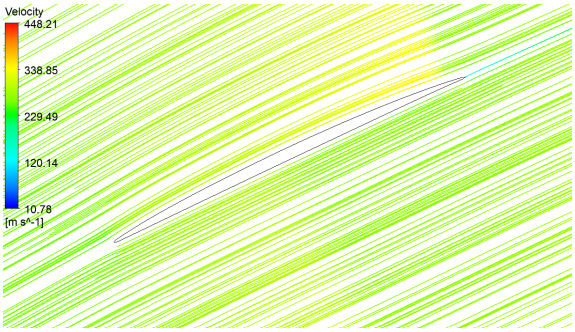

(d) Streamlines trend mid-span J3.5

Figure 3.18: Trend of the Mach number and streamlines around the mid-span profiles at M0.8, J2.9 and J3.5

For the near-tip profiles in figures 3.19a and 3.19b as already observed in the case at an advance ratio of J=3.06, one can observed that the flow tends to separate at the leading edge, but it reattaches soon towards the trailing edge.

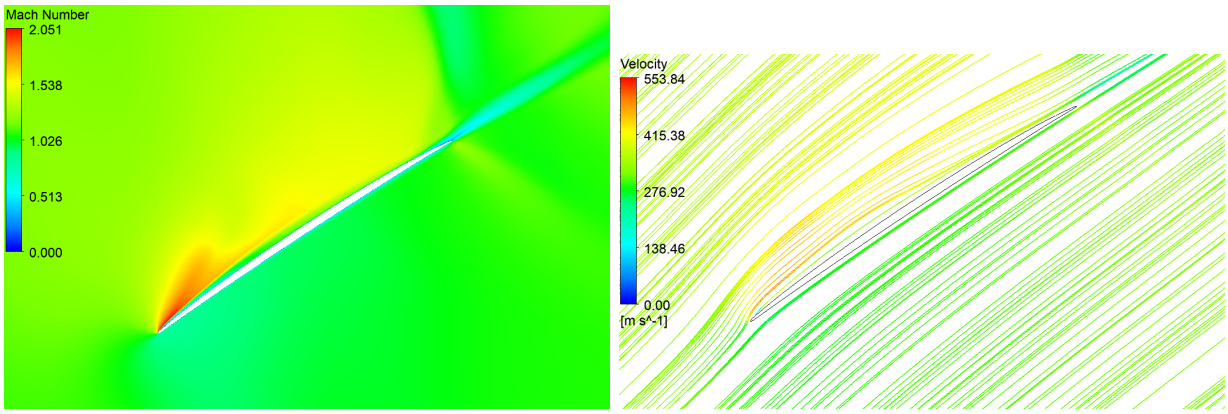

(a) Mach number trend near-tip J2.9 (b) Streamlines trend near-tip J2.9

Figure 3.19: Trend of the Mach number and streamlines around the near-tip profiles at M0.8 and J2.9

At the blade tip in the case of J=3.5 (3.20a and 3.20b), the flow does not separate, as it does instead in the cases of J=2.9 and J=3.06.

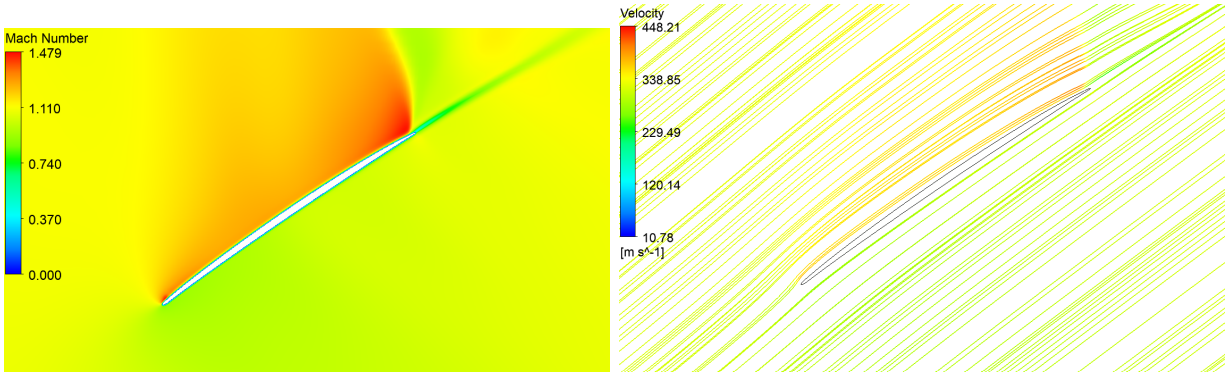

(a) Mach number trend at balde tip J3.5 (b) Streamlines trend at blade tip J3.5

Figure 3.20: Trend of the Mach number and streamlines around the blade tip profiles at M0.8 and J3.5

.

Finally, images of the vortex formed at the tip of the blade are shown for the advance ratios J=2.9, J=3.06 and J=3.5 respectively. It can be seen that the size of the vortex decreases as the advance ratio increases.

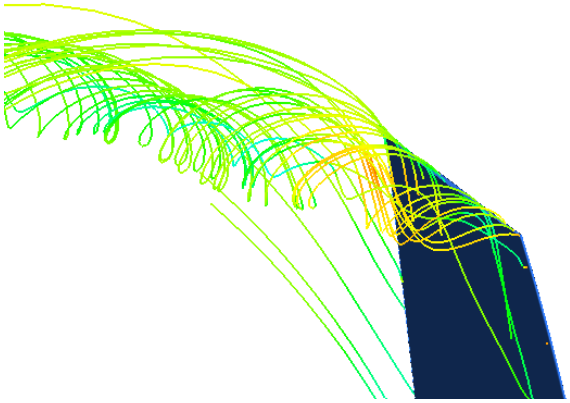

(a) Tip streamlines J=2.9

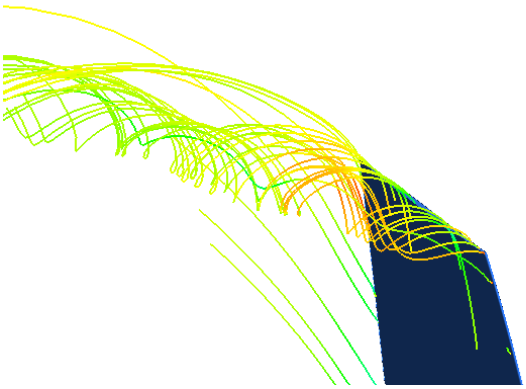

(b) Tip streamlines J=3.06

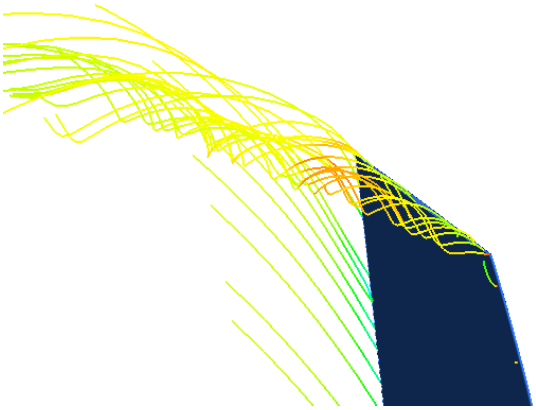

(c) Tip streamlines J=3.5

4 Conclusions

A CFD study regarding the NASA SR-3 propeller was conducted starting from the generation of a 3D model and performing a series of steady-state CFD analysis based on RANS equations with turbulence model $k-\omega$ SST. The results obtained show an overestimation of the power coefficient which affects efficiency. From NASA data, a maximum efficiency of 78.2% is observed, compared to the 70.9% obtained from the CFD analysis. The cause of the data discrepancy can be attributed to the deformation that the propeller undergoes under high loads and the lack of data related to the actual geometry produced. The difference in the power coefficient and efficiency decreases at high advance ratios and approaches the cases experienced by NASA. Other causes were related to the limitations of the CFD model. In fact, the analyses were carried-out with steady state assumptions, simulating only part of the propeller and using MRF-type interfaces. Simulations with the propeller rotating would better capture all the relevant phenomena while making the computational cost and simulation time higher. Further results were obtained from the comparison of the speed measurements at different spans of the blade exit. In the low-span and tip cases, the CFD analysis fairly reflected the trend of the velocities measured in the NASA tests. Potential future developments to improve the work done could involve analyzing the deformation through aeroelastic simulations, densifying the mesh, or performing time-varying analyses.

BIBLIOGRAPHY

[1] A. El-Sayed, "Aircraft propulsion and gas turbine engines," *Aircraft Propulsion and Gas Turbine Engines: Second Edition*, pp. 1–1477, 02 2008.

[2] R. Jeracki, D. Mikkelson, and B. Blaha, "Wind tunnel performance of four energy efficient propellers designed for mach 0.8 cruise," pp. 1–26, 05 1979.

[3] H. Neumann, L. Bober, J. Serafini, and L.-K. Chang, "An analytical and experimental comparison of the flow field of an advanced swept turboprop," *21st Aerospace Sciences Meeting*, pp. 1–17, 02 1983.

[4] C. Rohrbach, F. Metzger, D. Black, and R. Ladden, "Evaluation of wind tunnel performance testings of an advanced 45 deg swept 8-bladed propeller at mach numbers from 0.45 to 0.85," *NASA Contractor Reports*, pp. 1–134, 04 1982.

[5] J. D. Anderson, *Aircraft performance and design*. WCB/McGraw-Hill, 1999.

[6] J. Dittmar, R. Jeracki, and B. Blaha, "Tone noise of three supersonic helical tip speed propellers in a wind tunnel," *The Journal of the Acoustical Society of America*, vol. 68, pp. 1–23, 07 1979.

[7] T. Boulkeraa, A. Ghenaiet, and E. Benini, "Optimum operating parameters and blade setting of a high-speed propeller," *Journal of Aircraft*, vol. 59, pp. 1–18, 12 2021.

[8] O. Mehmed, K. Kaza, J. Lubomski, and R. Kielb, "Bending-torsion flutter of a highly swept advanced turboprop," *NASA Technical Memorandum 82975*, pp. 1–25, 02 1981.

[9] A. Zarri, J. Christophe, S. Moreau, and C. Schram, "Influence of swept blades on low-order acoustic prediction for axial fans," *Acoustics*, vol. 2, pp. 1–21, 11 2020.

[10] R. Hager and D. Vrabel, "Advanced turboprop project," pp. 0–120, 02 1988.

[11] F. Holste and W. Neise, "Noise source identification in a propfan model by means of acoustical near field measurements," *Journal of Sound and Vibration*, pp. 1–25, 01 1997.

[12] T. Elson, "Computational aerodynamics for open rotor tip vortex interaction noise prediction," pp. 1–225, 11 2015.

[13] J. Groeneweg and L. Bober, "Nasa advanced propeller research," *NASA Technical Memorandum 101361*, pp. 1–36, 02 1988.

[14] G. Stefko, L. Bober, and H. Neumann, "New test techniques and analytical procedures for understanding the behavior of advanced propellers," *NASA Technical Memorandum 83360*, pp. 1–25, 04 1983.

[15] J. Wright and J. Cooper, "Introduction to aircraft aeroelasticity and loads: Second edition," pp. 1–543, 02 2015.

[16] M. De Gennaro, D. Caridi, and C. Nicola, "Noise prediction of nasa sr2 propeller in transonic conditions," *AIP Conference Proceedings*, vol. 1281, pp. 167–170, 09 2010.

[17] C. Casarosa, "Meccanica del volo," *Meccanica del Volo*, pp. 3–601, 2010.

[18] D. Planchard, *SOLIDWORKS 2022 Quick Start*. SDC Publications, 2022.

[19] A. CFX-Solver, "Theory guide," *Release ll*, 2006.

[20] I. ANSYS, "Ansys turbogrid reference guide," *Release 2021 R2*, 2021.

[21] R. McDonald and J. Gloudemans, "Open vehicle sketch pad: An open source parametric geometry and analysis tool for conceptual aircraft design," pp. 1–32, 01 2022.

[22] P. Poll and M. Laboratory, "Full potential analysis and design of transonic propellers /," pp. 1–93, 02 1991.

[23] P. Alves, M. Silvestre, and P. Gamboa, "Aircraft propellers—is there a future?," *Energies*, vol. 13, p. 4157, 08 2020.

[24] NASA, "Sr-3 propeller model." `https://catalog.archives.gov/id/17423299`, 1978.

[25] NASA, "Sr-5 propeller model." `https://catalog.archives.gov/id/17499664`, 1978.

[26] Z. Czyż, P. Karpiński, K. Skiba, and M. Wendeker, "Wind tunnel performance tests of the propellers with different pitch for the electric propulsion system," *Sensors*, vol. 22, pp. 1–18, 12 2021.

[27] D. D. Remer, "Aircraft systems for pilots," pp. 1–855, 02 2017.

[28] MATLAB, *9.13.0.2080170 (R2022b) Update 1*. Natick, Massachusetts: The MathWorks Inc., 2022.

ACKNOWLEDGEMENT

The supervisor of this thesis was supported by the PHD@UNIPD programme of the Foundation Cariparo under the project ANTENORE-Advanced iNvestigaTion at off-dEsigN Operation of uhbpR Engines.